

1

# Snow Interception Relationships with 2 Meteorology and Canopy Structure in a 3 Subalpine Forest

4

5 **Authors:**

6 Alexander Charles Cebulski<sup>1</sup> (ORCID ID - 0000-0001-7910-5056)

7 John Willard Pomeroy<sup>1</sup> (ORCID ID - 0000-0002-4782-7457)

8 <sup>1</sup>Centre for Hydrology, University of Saskatchewan, Canmore, Canada

9 **Corresponding Author:** A. Cebulski, 50 Lincoln Park, Canmore, Alberta, Canada, T1W

10 3E9, alexcebowski@gmail.com

11 **Abstract:** Snow accumulation models differ in how snow interception and ablation processes  
12 are represented and thus their application to diverse climates and forest types is uncertain.  
13 Existing parameterizations of initial snow interception before unloading include inherently  
14 coupled canopy snow accumulation and ablation processes. This leads to difficulty in di-  
15 agnosing processes and adding possible errors to simulations when incorporated as canopy  
16 interception routines in models that already account for canopy snow ablation. This study  
17 evaluates the theory underpinning parameterizations of initial snow interception using high-  
18 temporal resolution and fine-scale measurements of throughfall for events with minimal snow  
19 ablation and redistribution in both the canopy and on the ground. The relationship between  
20 these throughfall measurements, event meteorology, and a novel lidar-based canopy structure  
21 measurement are assessed in two subalpine forest plots in the Canadian Rockies. Contrary

22 to existing theories, no association of canopy snow load or air temperature with interception  
23 efficiency was observed. Instead, canopy structure emerged as the primary factor governing  
24 snow accumulation. A wind-driven snowfall event demonstrated that non-vertical hydrometeor  
25 trajectories can significantly increase snow-leaf contact area, thereby enhancing initial intercep-  
26 tion before ablation. Prediction of interception efficiency for this event improved dramatically  
27 when adjusted for hydrometeor trajectory angle based on a wind speed at one-third of the  
28 canopy height. Snow-leaf contact area showed a high sensitivity to wind speed, increasing by  
29 up to 95% with a  $1 \text{ m s}^{-1}$  wind speed. The study proposes a new parameterization that calcu-  
30 lates throughfall, independent of processes that ablate snow from the canopy, as a function of  
31 snow-leaf contact area adjusted for hydrometeor trajectory angle. This new parameterization  
32 successfully estimated subcanopy snow accumulation for a snowfall event at two forest plots  
33 measured using lidar and snow surveys. By separating canopy snow ablation from snow inter-  
34ception processes, this new model offers potentially improved prediction of subcanopy snow  
35 accumulation when combined with canopy snow ablation parameterizations.

36 **Keywords:** snow interception, throughfall, ablation, forest, snowpack, lidar, process-based  
37 modelling

## 38 1 Introduction

39 Over half of North America's snow-covered zone is covered by forests (Kim et al., 2017), signif-  
40 icantly impacting the accumulation and redistribution of snowpacks and subsequent snowmelt  
41 runoff. Essery et al. (2003) estimated that 25–45% of annual snowfall may be lost to the atmo-  
42 sphere due to sublimation of snow intercepted in forest canopies globally. Snow intercepted  
43 in the canopy can sublimate and melt at much higher rates than the subcanopy snowpack  
44 (Katsushima et al., 2023; Lundberg & Halladin, 1994; Pomeroy et al., 1998), reducing the  
45 amount of snow available for runoff. Vegetation structure is one of the primary factors con-  
46 trolling the partitioning of snowfall into throughfall and interception (Hedstrom & Pomeroy,  
47 1998; Storck et al., 2002), and thus governs the quantity of snow subject to sublimation from

the canopy. However, forest thinning efforts aimed at limiting sublimation losses to increase snowmelt runoff do not always lead to a corresponding increase in spring streamflow (Golding & Swanson, 1978; Harpold et al., 2020; Pomeroy et al., 2012; Troendle, 1983). This may be due to increased ablation rates when forest cover is reduced, desynchronization of snowmelt, and sub-surface hydrology interactions (Ellis et al., 2013; Musselman et al., 2015; Pomeroy et al., 1997; Safa et al., 2021; Varhola et al., 2010). Given the significant impact of forest cover on snowpacks, along with the limited or absent monitoring networks for subcanopy snow accumulation (Rittger et al., 2020; Vionnet et al., 2021), land management, ecological conservation, and water resource decisions depend on reliable models of snow redistribution.

Hedstrom & Pomeroy (1998), working in the cold continental boreal forest, proposed that initial snow interception efficiency was controlled by the maximum canopy load which itself was a function of leaf area index and new snow density. Unloading was found to be an exponential function of time and observed only days or weeks after the interception event. Storck et al. (2002), working in temperate coastal forests, emphasized the role of leaf area index and air temperature in controlling the maximum canopy snow load. Gelfan et al. (2004) demonstrated accurate subcanopy snowpack simulations at study sites in Russia by treating the Hedstrom & Pomeroy (1998) and Storck et al. (2002) parameterizations separately while using a step-based function to choose either parameterization based on air temperature. A similar parameterization in the Cold Regions Hydrological Model (Pomeroy et al., 2022) has shown strong performance at sites across Canada, northern United States, Switzerland, and Spain. However, overestimation of subcanopy snow accumulation was reported by Lundquist et al. (2021) and Lumbrazo et al. (2022) when combining the Hedstrom & Pomeroy (1998) routine with ablation parameterizations from different studies (e.g., Roesch et al., 2001). The coupling of ablation processes within existing snow interception models (Hedstrom & Pomeroy, 1998; Storck et al., 2002) may contribute to overestimates of throughfall, canopy snow unloading, and canopy snow melt when combined with other canopy snow ablation parameterizations (Cebulski & Pomeroy, 2024). Additional observations of snow interception that exclude ablation processes could help determine the applicability of the interception theories proposed by

76 Hedstrom & Pomeroy (1998) and Storck et al. (2002). Hedstrom & Pomeroy's (1998) theory  
77 also suggests that moderate wind speeds, which can result in more horizontal hydrometeor tra-  
78 jectories, increasing snow-leaf contact area and interception efficiency at the plot scale. This  
79 association has also been shown in rainfall interception studies to decrease throughfall of rain  
80 (Herwitz & Slye, 1995; Van Stan et al., 2011). However, the relationship proposed by Hed-  
81 strom & Pomeroy (1998), is typically not included in snow accumulation models as empirical  
82 testing of this relationship is lacking.

83 The objective of this paper is to evaluate the theories underlying existing snow interception  
84 models using high spatial and temporal resolution measurements of subcanopy snow accumu-  
85 lation for events with minimal canopy snow ablation. These new observations are investigated  
86 to address the following research questions:

- 87 1. Are the existing theories regarding the relationships between meteorology and forest  
88 structure and initial snow interception supported by in-situ observations?
- 89 2. Is snow interception influenced by non-vertical hydrometeor trajectory angles over a  
90 wind-driven snowfall event?
- 91 3. To what extent can these findings inform the development of a new parameterization for  
92 snow interception?

## 93 **2 Theory**

### 94 **2.1 Snow interception**

95 The change in canopy snow load over time,  $\frac{dL}{dt}$  ( $\text{kg m}^{-2} \text{ s}^{-1}$ ), can be estimated from the mass  
96 balance:

$$\frac{dL}{dt} = q_{sf} + q_{ros} - q_{tf} - q_{unld} - q_{drip} - q_{wind}^{veg} - q_{sub}^{veg} \quad (1)$$

97 where  $q_{sf}$  is the snowfall rate ( $\text{kg m}^{-2} \text{ s}^{-1}$ ),  $q_{ros}$  ( $\text{kg m}^{-2} \text{ s}^{-1}$ ) is the rate of rainfall falling on  
 98 snow intercepted in the canopy,  $q_{tf}$  ( $\text{kg m}^{-2} \text{ s}^{-1}$ ) is the throughfall rate ( $\text{kg m}^{-2} \text{ s}^{-1}$ ),  $q_{unld}$  is  
 99 the canopy snow unloading rate ( $\text{kg m}^{-2} \text{ s}^{-1}$ ),  $q_{drip}$  is the canopy snow drip rate due to canopy  
 100 snowmelt ( $\text{kg m}^{-2} \text{ s}^{-1}$ ),  $q_{wind}^{veg}$  is the wind transport rate in or out of the control volume ( $\text{kg}$   
 101  $\text{m}^{-2} \text{ s}^{-1}$ ), and  $q_{sub}^{veg}$  is the intercepted snow sublimation rate ( $\text{kg m}^{-2} \text{ s}^{-1}$ ). During periods with  
 102 low air temperatures and low wind speeds,  $q_{ros}$ ,  $q_{unld}$ ,  $q_{drip}$ ,  $q_{wind}^{veg}$ , and  $q_{sub}^{veg}$  can be assumed  
 103 negligible. Figure 1 in Cebulski & Pomeroy (2024) presents a visual representation of this  
 104 mass balance.

105 Interception efficiency,  $\frac{I}{P}$  (-), which is the fraction of snowfall intercepted over  $\Delta t$  before  
 106 ablation, can be calculated as:

$$\frac{I}{P} = \frac{\Delta L}{q_{sf}\Delta t} \quad (2)$$

107 and throughfall,  $q_{tf}$  can be calculated as:

$$q_{tf} = \left(1 - \frac{I}{P}\right) \cdot q_{sf} \quad (3)$$

## 108 2.2 Hydrometeor trajectory angle

109 Herwitz & Slye (1995) calculate the trajectory angle of a hydrometeor,  $\theta_h$ , as the departure in  
 110 degrees ( $^\circ$ ) from a vertical plane as:

$$\theta_h = \arctan\left(\frac{x_h(u_z)}{v_h(D_h)}\right) * \frac{180}{\pi} \quad (4)$$

111 where  $v_h(D_h)$  is the terminal fall velocity of the hydrometeor ( $\text{m s}^{-1}$ ), which is a function of  
 112 the hydrometeor diameter,  $D_h$  and  $x_h(u_z)$  is the horizontal velocity of the hydrometeor ( $\text{m}$   
 113  $\text{s}^{-1}$ ) which is a function of the within canopy wind speed,  $u_z$  at height above ground,  $z$ . This  
 114 assumes the hydrometeors are following fluid points in the atmosphere.

<sup>115</sup> **3 Data and methods**

<sup>116</sup> **3.1 Study site**

<sup>117</sup> This study was conducted at Fortress Mountain Research Basin (FMRB), Alberta, Canada,  
<sup>118</sup> -115° W, 51° N, a continental headwater basin in the Canadian Rockies (Figure 1). Data from  
<sup>119</sup> this study was collected between October 2021 and July 2023 within and surrounding two  
<sup>120</sup> forest plots adjacent to the FMRB Powerline Station (PWL) and Forest Tower Station (FT)  
<sup>121</sup> at ~2100 m above sea level as shown in Figure 1. The average annual precipitation at PWL  
<sup>122</sup> Station from 2013 to 2023 was 1045 mm, with the peak annual snow water equivalent (SWE)  
<sup>123</sup> reaching 465 kg m<sup>-2</sup>, typically occurring in late April. The PWL and FT forest plots include  
<sup>124</sup> discontinuous stands of 70% subalpine fir (*Abies lasiocarpa*) and 30% Engelmann spruce (*Picea*  
<sup>125</sup> *engelmannii*) (Langs et al., 2020). The PWL plot is located 120 m to the northwest of FT  
<sup>126</sup> station and contains a forest clearing with a diameter of ~12 m, surrounded by a closed canopy.  
<sup>127</sup> The FT plot has a discontinuous canopy without artificial clearings. The canopy coverages of  
<sup>128</sup> the two forest plots are 0.51 and 0.29 and the winter leaf area indices are 2.07 and 1.66 for  
<sup>129</sup> PWL and FT respectively. The average height of the canopy surrounding the plot to the east  
<sup>130</sup> of the PWL station is 10.5 m and surrounding the forest plot around the FT Station is 7.1  
<sup>131</sup> m. In August of 1936, the majority of vegetation in FMRB burned during a large forest fire  
<sup>132</sup> that affected most of the Kananaskis Valley (Fryer et al., 1988). Following the fire, the forest  
<sup>133</sup> within the PWL and FT forest plots has naturally regenerated, though some trees have been  
<sup>134</sup> removed for road clearing and creation of a snow study plot.

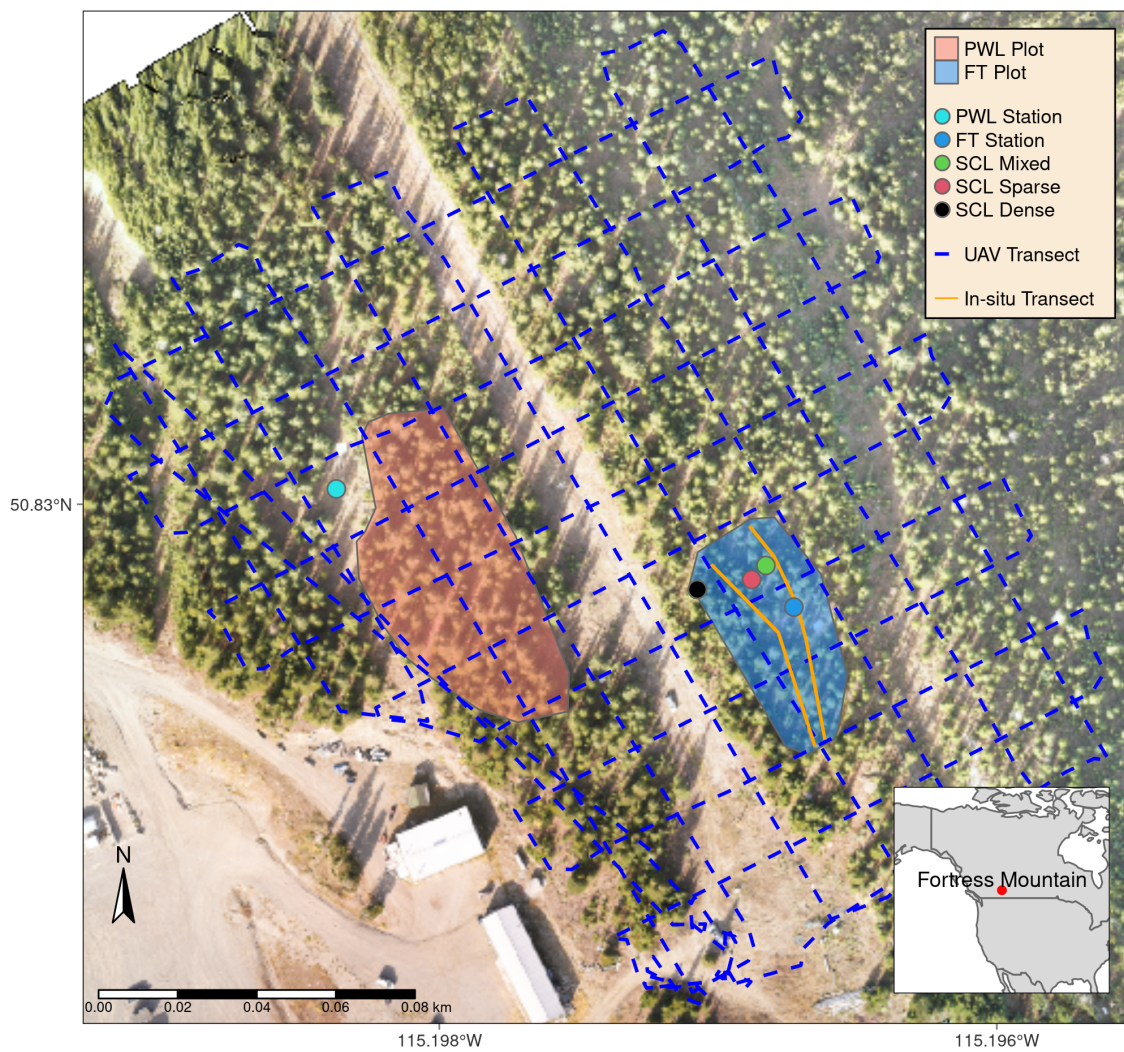


Figure 1: Map showing the location of forest plots, flux towers, subcanopy lysimeter instruments (SCL), and survey transects. The inset map on the lower right shows the regional location of Fortress Mountain Research basin.

<sup>135</sup> **3.2 Meteorological measurements**

<sup>136</sup> Measurements of air temperature and relative humidity (Vaisala model HMP155A), wind speed  
<sup>137</sup> and direction (RM Young model 86000 2-D ultrasonic anemometer) were made 4.3 m above the  
<sup>138</sup> ground at FT station (Figure 1). Wind speed measurements from a 3-cup anemometer (Met  
<sup>139</sup> One model 014A), installed adjacent to the 2-D ultrasonic anemometer at 4.3 m, were used for  
<sup>140</sup> gap filling wind speed. Additional wind speed measurements were collected by two 3D sonic  
<sup>141</sup> anemometers (Campbell Scientific CSAT3) installed at 2 m (raised to 3 m February 2022) and  
<sup>142</sup> 13.5 m above the ground at FT station. Average wind speeds at these three heights were found  
<sup>143</sup> to follow a logarithmic relationship. Thus, a wind profile was fitted to these measurements  
<sup>144</sup> using the Prandtl-von Kármán log-linear relationship:

$$\bar{u} = \frac{u_*}{k} \ln\left(\frac{z - d_0}{z_0}\right) \quad (5)$$

<sup>145</sup> where  $\bar{u}$  is average wind speed ( $\text{m s}^{-1}$ ) at height,  $z$  (m) above the ground,  $u_*$  is the friction  
<sup>146</sup> velocity ( $\text{m s}^{-1}$ ),  $d_0$  is the displacement height (m),  $z_0$  is the roughness length of momentum  
<sup>147</sup> (m), and  $k$  is the dimensionless von Kármán Constant (0.4).

<sup>148</sup> Using wind speed measurements at three heights at FT station, collected during events when  
<sup>149</sup> the instruments were confirmed to be free of snow, the function ‘optim’ from the ‘stats’ R  
<sup>150</sup> package (R Core Team, 2024) was used to estimate the values  $d_0$  and  $z_0$  for Equation 5 that  
<sup>151</sup> best fit the observed mean wind speed. The parameters found for the wind speed profile  
<sup>152</sup> include a  $d_0$  of 0.58 m and  $z_0$  of 0.50 m. See the supporting information for more information  
<sup>153</sup> on the development and testing of the wind profile.

<sup>154</sup> At PWL station, the snowfall rate was measured by an Alter-shielded OTT Pluvio weighing  
<sup>155</sup> precipitation gauge 2.6 m above ground, corrected for undercatch following phase correction  
<sup>156</sup> by Harder & Pomeroy (2013) and catch efficiency by Smith (2007). Wind speed for undercatch  
<sup>157</sup> correction was measured by a 3-cup anemometer (Met One model 014A) at a height of 2.6 m at  
<sup>158</sup> PWL station. An optical disdrometer (OTT Parsivel2) provided measurements of hydrometeor

<sup>159</sup> particle size and vertical velocity. All measurements were recorded at 15-min intervals using  
<sup>160</sup> Campbell Scientific dataloggers, except the Parsivel2 which was recorded at 1-minute intervals  
<sup>161</sup> by an onsite computer.

<sup>162</sup> **3.3 Lysimeter measurements**

<sup>163</sup> Three subcanopy lysimeters (SCLs) were installed surrounding the FT Station (Figure 1) to  
<sup>164</sup> provide 15-minute interval measurements of throughfall as in MacDonald (2010). Figure 2  
<sup>165</sup> shows the three SCLs which consisted of a plastic horse-watering trough with an opening of  
<sup>166</sup> 0.9 m<sup>2</sup> and depth of 20 cm suspended from a load cell (Intertechnology 9363-D3-75-20T1)  
<sup>167</sup> attached to an aluminum pipe connected between two trees. For 26 distinct snowfall events,  
<sup>168</sup> where canopy snow ablation rates were deemed negligible, snow captured in the SCLs was  
<sup>169</sup> assumed to be throughfall. The throughfall rate,  $q_{tf}$ , was calculated by dividing the weight  
<sup>170</sup> of snow in the SCL by the cross-sectional area of the SCL opening and determining the rate  
<sup>171</sup> of change at 15-minute intervals. Canopy snow load was estimated at the same 15-minute  
<sup>172</sup> intervals during these events using Equation 1 and incorporating measurements of  $q_{tf}$  from  
<sup>173</sup> the SCLs and  $q_{sf}$  from the PWL snowfall gauge. Rates of  $q_{ros}$ ,  $q_{unld}$ ,  $q_{drip}$ ,  $q_{wind}^{veg}$ , and  $q_{sub}^{veg}$   
<sup>174</sup> were assumed to be zero for these periods. Interception efficiency was also calculated for  
<sup>175</sup> these intervals using Equation 2. Timelapse imagery, mass change on a weighed tree lysimeter  
<sup>176</sup> “hanging tree” (Pomeroy & Schmidt, 1993) and in-situ observations were used to ensure the  
<sup>177</sup> ablation of snow intercepted in the canopy was minimal over each interval. Additionally,  
<sup>178</sup> the  $q_{tf}$  measurements were filtered to include observations with a snowfall rate  $> 0 \text{ kg m}^{-2}$   
<sup>179</sup> hr<sup>-1</sup>, throughfall rate  $> 0.05 \text{ kg m}^{-2} \text{ hr}^{-1}$  and a snowfall rate greater than the SCL measured  
<sup>180</sup> throughfall rate to minimize observations with unloading. The weighed tree lysimeter, a live  
<sup>181</sup> subalpine fir (*Abies lasiocarpa*) tree suspended from a load cell (Artech S-Type 20210-100)  
<sup>182</sup> measured the weight of canopy snow load (kg). This weight was scaled to an areal estimate of  
<sup>183</sup> canopy snow load ( $L$ , kg m<sup>-2</sup>) using measurements of areal throughfall (kg m<sup>-2</sup>) from manual  
<sup>184</sup> snow surveys and snowfall from the PWL Station snowfall gauge (see description of method  
<sup>185</sup> in Pomeroy & Schmidt, 1993). The canopy structure surrounding three SCLs is shown in

<sup>186</sup> Figure 2 and was measured using hemispherical photography (Nikon Coolpix 4500 and EC-F8  
<sup>187</sup> hemispherical lens) and the hemispheR R package Chianucci & Macek (2023). The leaf area  
<sup>188</sup> index and canopy coverage from hemispherical photo analysis is shown in Table 1.

Table 1: Canopy structure of the three subcanopy lysimeters (SCL) located proximal to the FT Station. Leaf area index (LAI) and Canopy Coverage was measured using hemispherical photo analysis with the R package hemispheR.

Name	LAI (-)	Canopy Coverage (-)
Sparse	1.59	0.73
Mixed	1.86	0.78
Closed	2.11	0.82

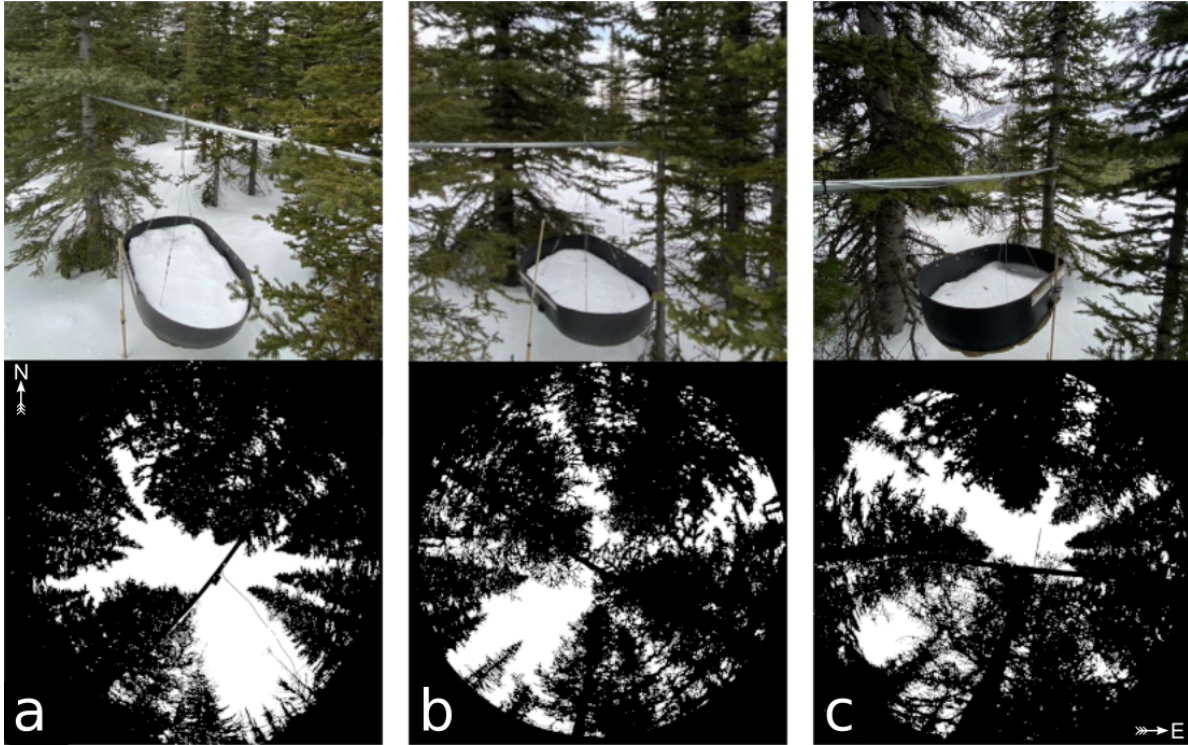


Figure 2: Images of the three subcanopy lysimeters (SCL) and surrounding canopy located in sparse (a), mixed (b), and dense (c) canopy. The top row presents a side view of each SCL and the bottom row shows hemispherical photographs classified using the hemispheR R package. These hemispherical images are oriented with north at the top and have been flipped to provide a view from above (i.e., east is on the right side of each image). See Table 1 for the canopy structure measurements of the canopy above each SCL.

### **189 3.4 UAV-Lidar data collection and processing**

**190** The UAV (FreeFly Alta X) payload included a REIGL miniVUX-2 airborne laser scanner,  
**191** an Applanix APX-20 inertial measurement unit (IMU) and global navigation satellite system  
**192** (GNSS). The UAV was flown 90 m above the ground at a speed of  $3 \text{ m s}^{-1}$  following the  
**193** path shown in Figure 1. A detailed description of the UAV, payload, and flight settings is  
**194** provided in the supporting information. The methods outlined by Harder et al. (2020) and  
**195** Staines & Pomeroy (2023) were incorporated to reconcile survey lidar, IMU and GNSS data.

196 A systematic vertical bias of up to 6 cm between UAV-lidar flight lines was observed in the  
197 resulting point clouds on March 13<sup>th</sup> and 14<sup>th</sup>, 2024 and was attributed to IMU position  
198 drift. This offset between flight lines was corrected using the BayesStripAlign software v2.24  
199 (BayesMap Solutions, 2024). After strip alignment, the mean elevation bias in the point clouds  
200 was 0.000 m and the RMS error declined from 0.055 m to 0.038 m on March 13<sup>th</sup> and changed  
201 from 0.033 m to 0.029 m on March 14<sup>th</sup>. The point cloud density ranged from ~1200 returns m<sup>2</sup>  
202 in sparse forest to ~2200 returns m<sup>2</sup> in open clearings. Quality control, ground classification,  
203 calculation of surface elevation change (subtraction of the two UAV-lidar point clouds), and  
204 generation of 0.05 m resolution rasters was conducted using the LAStools software package  
205 (LAStools, 2024). Post processing and resampling of raster data to a 0.25 m grid cell resolution  
206 was conducted using the ‘Terra’ R package (Hijmans, 2024). More details on the UAV-lidar  
207 processing workflow are provided in the supporting information.

## 208 3.5 Snow surveys

### 209 3.5.1 In-situ snow depth and density

210 Twelve in-situ fresh snow surveys (six pre- and post-snowfall event pairs) provided measure-  
211 ments of subcanopy throughfall depth and density at 30 locations following the transects shown  
212 in Figure 1 to upscale the weighed tree snow load from kg to kg m<sup>-2</sup> as in Pomeroy & Schmidt  
213 (1993). Minimal ablation and redistribution of snow was observed between the pre- and post-  
214 snowfall surveys. When conditions allowed for a UAV-lidar flight, the in-situ snow surveys  
215 were conducted following the UAV-lidar flight to assess the accuracy of the throughfall mea-  
216 surements and provide a fresh snow density for the calculation of SWE (kg m<sup>-2</sup>). A 1000 cm<sup>3</sup>  
217 Perla snow density wedge sampler (RIP Cutter, [https://snowmetrics.com/shop/rip-1-cutter-](https://snowmetrics.com/shop/rip-1-cutter-1000-cc/)  
218 1000-cc/) was used to measure the density of the fresh snow layer,  $\rho_{tf}$  (kg m<sup>-3</sup>) from snow  
219 pits. Throughfall depth measurements,  $\Delta HS$  were converted to SWE using the following  
220 equation:

$$\Delta SWE_{tf} = \Delta HS \cdot \overline{\rho_{tf}} \quad (6)$$

221 Differential GNSS rover coordinates, with  $\pm 2.5$  cm 3D uncertainty, were taken at each snow  
222 sampling location so the locations could be queried later from the UAV-lidar rasters to assess  
223 measurement error and were also used as input for the UAV-lidar strip alignment. If a pre-  
224 event crust layer was present, the depth of post event fresh snow accumulation above the crust  
225 layer was interpreted as throughfall over the event. In the absence of a defined crust layer, the  
226 difference in pre- and post-event snow depth to ground was interpreted as event throughfall.

227 **3.5.2 UAV-Lidar snow depth**

228 Two uncrewed aerial vehicle (UAV) lidar surveys were conducted before and after a 24-hour  
229 snowfall event that occurred between March 13<sup>th</sup> and March 14<sup>th</sup>, 2023 to facilitate the mea-  
230 surement of snow accumulation and canopy structure within the FT and PWL forest plots.  
231 This period was selected based on two criteria: 1) it provided sufficient cumulative snowfall  
232 to result in a low relative error in UAV-lidar measured throughfall, and 2) minimal snow  
233 redistribution and ablation was observed, as confirmed by the SCLs, weighed tree, and time-  
234 lapse imagery. The change in surface elevation between the two UAV-lidar point clouds was  
235 interpreted as the increase in snow accumulation,  $\Delta HS$  over the snowfall event.

236 **3.6 UAV-Lidar canopy metrics**

237 The canopy structure in the two UAV-lidar point clouds (March 13<sup>th</sup> and March 14<sup>th</sup>) was  
238 characterized using the voxel ray sampling (VoxRS) methodology for lidar data analysis, as  
239 developed by Staines & Pomeroy (2023). This method was chosen for its ability to provide  
240 canopy metrics that are less sensitive to the inherent non-uniform nature of lidar sampling data,  
241 which often results from beam occlusion in vegetation and leads to reduced points near the  
242 ground. Using this method radiation transmittance,  $\tau (-)$ , was measured across the hemisphere

243 at a  $1^\circ$  step, i.e., azimuth angles ( $0^\circ, 1^\circ, \dots, 359^\circ$ ) and zenith angles ( $0^\circ, 1^\circ, \dots, 90^\circ$ ) for each  
244 0.25 m grid cell within the FT and PWL forest plots. The fraction of snow-leaf contact area  
245 per unit area of ground proposed by Hedstrom & Pomeroy (1998), and hereafter called leaf  
246 contact area ( $C_p$ ), was then calculated as:

$$C_p(C_c, \theta_h, L) = 1 - \tau \quad (7)$$

$$C_p(C_c, \theta_h, L) = \begin{cases} 1 - \tau, & \text{if } \theta_h > 0^\circ \\ 1 - \tau \approx C_c, & \theta_h = 0^\circ \end{cases} \quad (8)$$

247 where  $C_p$  is a function of the canopy coverage  $C_c$ ,  $\theta_h$  and  $L$ .  $C_p$  is approximately equal to  
248 canopy coverage ( $C_c$ ) for vertical snowfall trajectories.

249 **3.7 Statistics and regression models**

250 To determine how forest structure was associated with interception efficiency at different az-  
251 imuth and zenith angles over the March 13–14 snowfall event, the entire hemisphere at each  
252 grid location was considered. The relationship between interception efficiency and  $C_p$  was  
253 found to be linear and thus the Pearson Correlation Coefficient,  $\rho_p$  was calculated using the  
254 ‘stats’ package in R (R Core Team, 2024). The  $\rho_p$  was computed between a single raster of  
255 interception efficiency and each of the 32,760 rasters of  $C_p$ , representing locations across the  
256 hemisphere (azimuth [ $0^\circ, 1^\circ, \dots, 359^\circ$ ], zenith angle [ $0^\circ, 1^\circ, \dots, 90^\circ$ ]) at 0.25 m grid cells spanning  
257 the FT and PWL forest plots.

258 Linear and non-linear regression models were developed to assess relationships in the observed  
259 data. Linear models were fitted using ordinary least squares regression via the ‘lm’ function  
260 from the R ‘stats’ package (R Core Team, 2024) to analyze two relationships: (1) between  
261 interception efficiency and meteorological variables and (2) between interception efficiency and  
262 leaf contact area. The latter was forced through the origin based on the theoretical justification

that the dependent variable should be zero when the independent variable is zero. Kozak & Kozak (1995) noted, the default  $R^2$  value provided for least squares models forced through the origin by many statistical packages can be misleading. Therefore, these  $R^2$  values were adjusted using Equation 10 in Kozak & Kozak (1995). Non-linear models were fitted to investigate the relationship of leaf contact area with simulated trajectory angle using non-linear least squares regression via the ‘nls’ function in ‘stats’ package in R.

## 4 Results

### 4.1 The influence of meteorology on snow interception

Canopy snow load was estimated for 26 snowfall events and increased linearly with cumulative event snowfall without evidence of reaching a maximum (Figure 3). Over these events, air temperature ranged from -24.5°C to 1°C, wind speeds at 4.3 m height ranged from calm to  $4.6 \text{ m s}^{-1}$  (Table 2), and wind direction was predominately from the southwest during snowfall (Figure 4). Missing canopy snow load measurements in Figure 3 for certain troughs during specific events was caused by damage to the subcanopy lysimeter wiring due to animals and heavy snow loads.

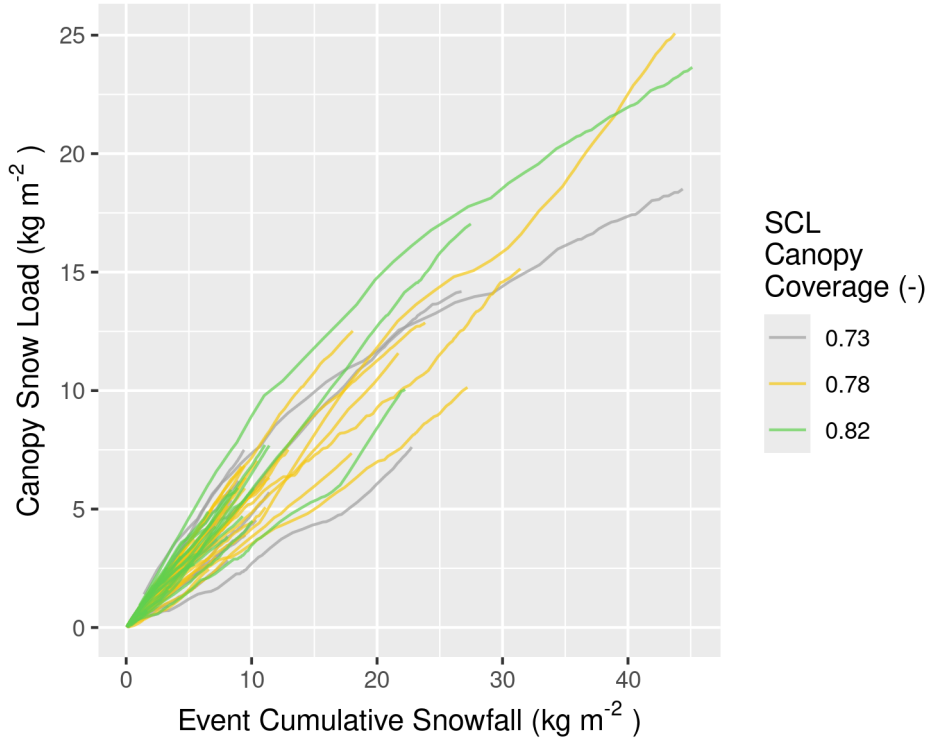


Figure 3: Plot showing the cumulative event snowfall versus the corresponding state of canopy snow load calculated using the subcanopy lysimeters (SCLs) for each of the 26 snowfall events. The SCLs are denoted by a distinct colour (grey, yellow, and green), correspond to varying canopy coverage (0.73, 0.78, and 0.82, respectively).

Table 2: Meteorology of the 26 snowfall events. Air temperature and wind speed were measured at FT station. Interception efficiency is estimated from snowfall measured at PWL station and the average throughfall of all three SCLs located within the FT forest plot (all from 15-min. measurements).

Start Date	Air Temperature (°C)			Wind Speed (m/s)			Interception Efficiency (-)			Snowfall (kg m <sup>-2</sup> )
	Min	Mean	Max	Min	Mean	Max	Min	Mean	Max	
2021-12-23	-6.2	-5.3	-4.6	0.6	3.1	4.6	0.7	0.8	1.0	21.7
2022-01-02	-15.9	-10.6	-5.8	0.2	1.9	4.2	0.1	0.7	1.0	32.9
2022-01-17	-14.8	-7.8	-0.8	0.2	1.1	1.8	0.0	0.6	1.0	12.9
2022-01-31	-24.5	-12.1	-6.4	0.1	1.0	1.7	0.2	0.7	1.0	9.1
2022-02-14	-9.9	-9.0	-8.5	0.4	0.8	1.2	0.2	0.5	0.8	1.7
2022-02-19	-4.7	-3.2	-2.5	1.3	2.3	3.6	0.3	0.6	0.9	11.1
2022-03-01	-8.3	-5.4	-1.0	0.1	1.0	3.1	0.4	0.8	1.0	9.9
2022-03-07	-12.5	-8.6	-4.4	0.3	0.8	1.7	0.3	0.7	1.0	9.5
2022-03-14	-2.7	-2.1	-0.8	1.0	1.6	2.9	0.2	0.6	0.9	8.4
2022-03-19	-3.1	-2.8	-2.5	0.0	0.7	1.3	0.3	0.5	0.6	6.6
2022-03-23	-7.9	-5.3	-0.9	0.8	1.2	1.8	0.4	0.6	0.9	1.6
2022-04-04	-3.5	-2.9	-2.1	0.6	1.0	1.9	0.0	0.4	0.6	3.4
2022-04-18	-5.2	-4.0	-2.7	0.4	1.1	1.9	0.1	0.5	0.9	7.4
2022-04-22	-2.8	-1.8	-0.5	0.4	0.8	1.2	0.1	0.5	1.0	9.8
2022-05-09	-4.9	-4.3	-3.2	0.1	0.4	0.9	0.2	0.5	0.9	8.1
2022-05-19	-4.9	-2.1	0.3	0.1	0.4	0.9	0.2	0.6	0.9	7.1
2022-06-13	-1.1	-0.3	0.6	0.1	0.1	0.4	0.0	0.5	0.9	45.3
2022-12-27	-3.0	-2.7	-1.9	0.6	1.1	1.8	0.2	0.5	0.9	4.5
2023-01-27	-11.5	-7.3	-4.5	0.6	0.9	1.2	0.1	0.5	0.8	10.4
2023-02-19	-14.3	-9.5	-6.3	0.2	0.8	1.4	0.2	0.7	1.0	18.1
2023-02-26	-9.2	-8.4	-6.6	0.2	1.0	2.1	0.3	0.5	1.0	5.4
2023-03-13	-8.9	-3.6	-0.1	0.3	1.3	2.2	0.0	0.5	1.0	27.4
2023-03-24	-7.9	-5.7	-3.5	0.1	0.5	1.2	0.1	0.4	0.7	23.8
2023-04-01	-8.9	-7.7	-4.7	0.1	0.6	1.4	0.4	0.6	0.8	11.4
2023-04-10	-1.1	-0.5	0.3	0.1	0.3	1.0	0.2	0.4	0.6	18.0
2023-05-08	0.2	0.6	1.0	0.4	0.6	0.8	0.6	0.6	0.7	3.5

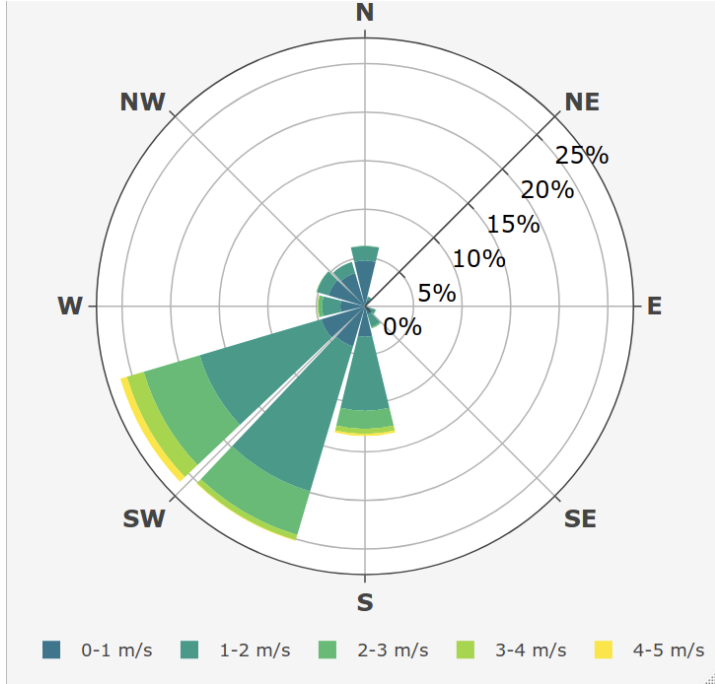


Figure 4: Wind rose showing the frequency of wind speed and direction over the 26 snowfall periods for the ultrasonic anemometer 4.3 m above ground at FT station.

Event average air temperature and interception efficiency were negatively associated for the mixed canopy ( $R^2 = 0.1$ ,  $p < 0.05$ ), but not associated at the closed and sparse canopies (Table 3 & Figure 5). Cumulative event snowfall was not associated with event interception efficiency at any site ( $p > 0.05$ ). Event wind speed was positively associated with interception efficiency for the sparse ( $R^2 = 0.1$ ,  $p > 0.05$ ) and closed ( $R^2 = 0.2$ ,  $p < 0.05$ ) canopies, both with limited canopy openings (Figure 2a,c) towards the prevailing wind direction shown in the wind rose in Figure 4. However, interception efficiency in the mixed canopy, which is partially open towards the prevailing wind direction, was not associated with wind speed ( $p > 0.05$ ).

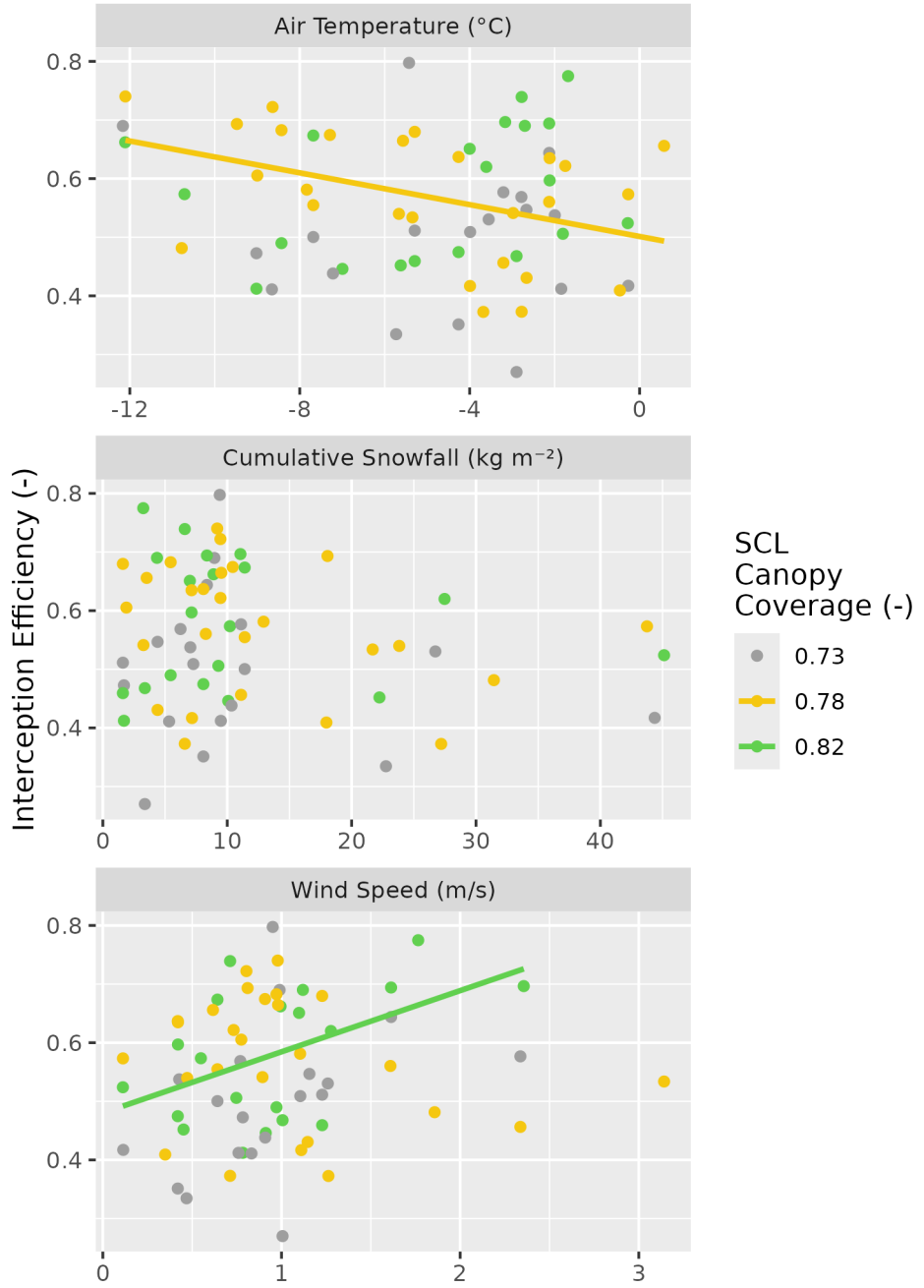


Figure 5: Scatter plots showing the event mean air temperature, mean wind speed, and cumulative snowfall versus the event mean interception efficiency estimated using the SCLs for each of the 26 snowfall events. The colours (grey, yellow, and green), correspond to varying canopy coverage (0.73, 0.78, and 0.82, respectively). A linear regression line fit to the data for significant relationships ( $p < 0.05$ ) is shown by the solid coloured lines. See Table 3 for linear regression statistics.

Table 3: Statistics corresponding to the ordinary least squares linear regression test between independent variables: mean event air temperature, cumulative event snowfall, and mean event wind speed, and the dependent variable mean event interception efficiency. The test was run separately for three levels of canopy coverage ( $C_c$ ).

SCL					
Dependent Variable	Name	$C_c$	Adjusted $R^2$	p-value	n
Air Temperature (°C)	Sparse	0.73	-0.032	0.519	19
Air Temperature (°C)	Mixed	0.78	0.141	0.033	26
Air Temperature (°C)	Closed	0.82	0.008	0.297	20
Cumulative Snowfall (kg m <sup>-2</sup> )	Sparse	0.73	-0.038	0.568	19
Cumulative Snowfall (kg m <sup>-2</sup> )	Mixed	0.78	0.030	0.197	26
Cumulative Snowfall (kg m <sup>-2</sup> )	Closed	0.82	-0.049	0.732	20
Wind Speed (m/s)	Sparse	0.73	0.114	0.087	19
Wind Speed (m/s)	Mixed	0.78	0.010	0.275	26
Wind Speed (m/s)	Closed	0.82	0.192	0.030	20

286 Fifteen-minute interval measurements of interception efficiency and air temperature shown  
 287 in Figure 6a were not associated, despite significant relationships for the sparse and mixed  
 288 canopies ( $R^2 < 0.03$ ,  $p < 0.05$ ), due to low predictive power (Table 4). The average interception  
 289 efficiency across differing bins of air temperature also does not show any systematic trend  
 290 (Figure 6a). However, a significantly greater median interception efficiency ( $p < 0.05$ ) was  
 291 found for binned measurements with air temperatures below -6 °C compared to those with  
 292 warmer air temperatures using non-parametric Wilcoxon signed rank test.

293 Mean wind speed was weakly associated with interception efficiency for the sparse ( $R^2 = 0.1$ ,  $p$   
 294 > 0.05) and closed ( $R^2 = 0.2$ ,  $p < 0.05$ ), but not for the mixed canopy ( $p > 0.05$ ) (Table 4). The  
 295 binned data show an increasing trend in interception efficiency with increasing wind speed for  
 296 the sparse and closed canopies (Figure 6b). A comparison of interception efficiencies binned for  
 297 low (< 1 m s<sup>-1</sup>) and high (> 1 m s<sup>-1</sup>) wind speeds by the Wilcoxon signed rank test, showed that

298 high wind speeds had significantly higher ( $p < 0.05$ ) median interception efficiencies compared  
299 to the low wind speed bins for the closed and sparse canopy. Conversely, the Wilcoxon test  
300 showed the mixed canopy, which had an opening in the canopy towards the prevailing wind  
301 direction (Figure 2b), had significantly higher ( $p < 0.05$ ) median interception efficiencies for  
302 the low wind speed bins.

303 Interception efficiency showed no association ( $R^2 < 0.05$ ,  $p > 0.2$ ) with the canopy load mea-  
304 sured at the beginning of the 15-minute intervals (Table 4). The binned data show a small  
305 increase in interception efficiency for all three canopies when the snow load is less than  $7 \text{ kg m}^{-2}$   
306 (Figure 6c). Interception efficiency later declined for snow loads greater than  $7 \text{ kg m}^{-2}$  for all  
307 canopies, though this was inconsistent for the mixed canopy. A significantly greater ( $p < 0.05$ )  
308 median interception efficiency was found for canopy snow loads less than  $10 \text{ kg m}^{-2}$  than those  
309 with high initial canopy snow loads ( $> 10 \text{ kg m}^{-2}$ ) using the Wilcoxon rank-test. Additional  
310 statistics from ordinary least squares regression test on the 15-minute interval measurements  
311 are provided in Table 4.

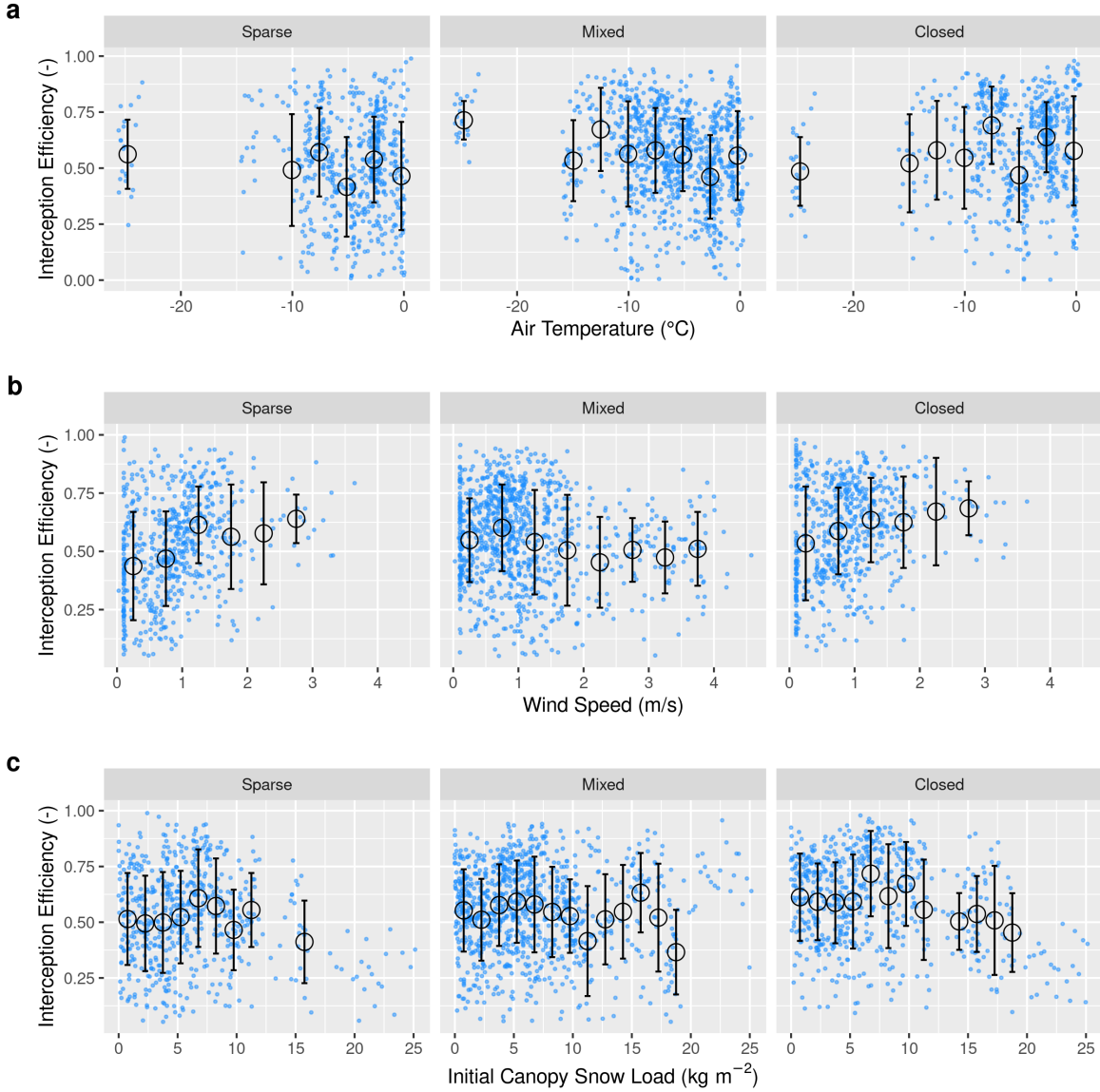


Figure 6: Scatter plots of 15-minute interval measurements (blue dots) and binned data (black open circles with error bars) of mean air temperature, mean wind speed, and initial canopy snow load versus mean snow interception efficiency. Panels show (a) air temperature, (b) wind speed, and (c) initial canopy snow load (the snow load observed at the beginning of the timestep). The black open circles show the mean of each bin and the error bars represent the standard deviations. See Table 4 for linear regression statistics.

Table 4: Statistics corresponding to the ordinary least squares linear regression test between 15-minute interval measurements of independent variables: mean air temperature, mean wind speed, and initial canopy snow load and the dependent variable mean interception efficiency. The test was run separately for three levels of canopy coverage ( $C_c$ ).

Dependent Variable		SCL	$C_c$	Adjusted $R^2$	p-value	n
Air Temperature (°C)	Mixed	0.78	0.032	0.000	985	
Air Temperature (°C)	Closed	0.82	0.004	0.069	618	
Air Temperature (°C)	Sparse	0.73	0.007	0.019	603	
Wind Speed (m/s)	Mixed	0.78	0.017	0.000	985	
Wind Speed (m/s)	Closed	0.82	0.037	0.000	618	
Wind Speed (m/s)	Sparse	0.73	0.089	0.000	603	
Initial Canopy Snow Load (kg m <sup>-2</sup> )	Mixed	0.78	0.000	0.453	972	
Initial Canopy Snow Load (kg m <sup>-2</sup> )	Closed	0.82	0.051	0.000	607	
Initial Canopy Snow Load (kg m <sup>-2</sup> )	Sparse	0.73	0.025	0.000	592	

## 4.2 The influence of forest structure on snow interception

UAV-lidar measurements of throughfall and canopy structure provide insights on how the forest canopy influenced subcanopy snow accumulation during a wind-driven snowfall event between March 13<sup>th</sup> and 14<sup>th</sup> 2023. This event totaled 28.7 kg m<sup>-2</sup> of snowfall at PWL station and was characterized by a transition from low rates of snowfall and air temperatures near 0°C to higher rates of snowfall by late afternoon on March 13<sup>th</sup> coinciding with air temperatures around -2.5 °C. An average wind speed of 1.3 m s<sup>-1</sup> and direction of 188° was observed 4.3 m above the ground at FT Station. Figure 7 shows Cionco's (1965) exponential function for within canopy wind speed was not appropriate for this sparse canopy. The predicted hydrometeor trajectory angles at varying heights, calculated using Equation 4 and the mean observed hydrometeor terminal velocity observed over the event of 0.9 m s<sup>-1</sup> are also shown in Figure 7. An average

323 wind speed of  $1.6 \text{ m s}^{-1}$  and direction of  $188^\circ$  was calculated by integrating the wind speed  
 324 from the surface to the mean canopy height of FT plot. The corresponding trajectory angle  
 325 calculated using Equation 4 from this integrated wind speed was  $61.5^\circ$ .

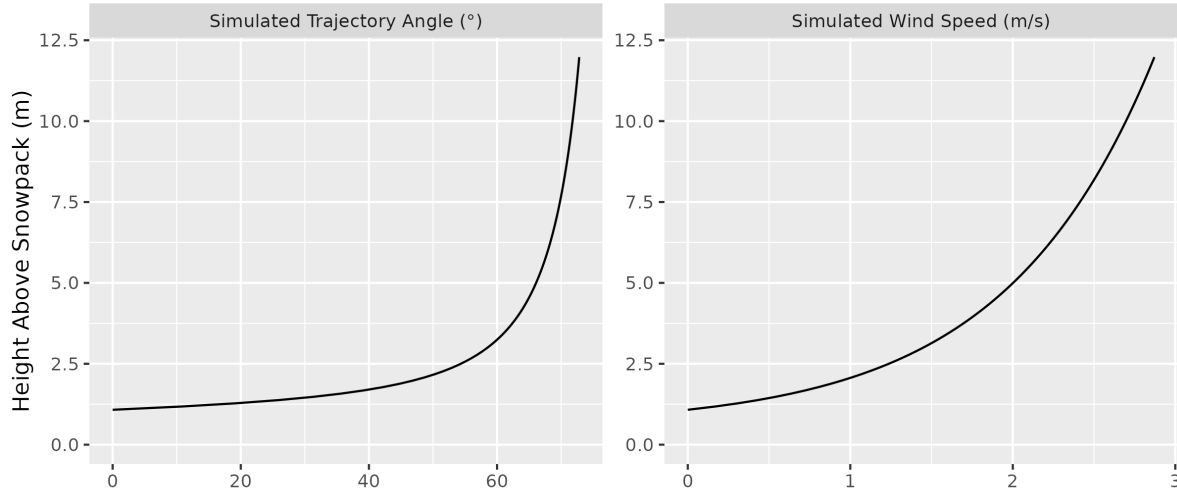


Figure 7: Wind speed profile using roughness length and displacement height parameters derived from anemometers at 2, 3, 4.3, and 13.5 m above ground at FT station over snow free periods and friction velocity estimated over the March 13–14<sup>th</sup> snowfall event.

326 Throughfall depth measured by UAV-lidar was close to the 28 in-situ manual measurements  
 327 with a mean bias of -0.001 m and RMSE of 0.024 m. More details on the accuracy of UAV-lidar  
 328 snowdepth measurements are provided in the supporting information section. Figure 8 shows  
 329 the spatial distribution of throughfall and interception efficiency at the PWL and FT forest  
 330 plots. Reduced throughfall and greater interception efficiency was observed on the north (lee)  
 331 side of individual trees, which may be due to non-vertical hydrometeor trajectories caused by  
 332 the steady southerly winds observed over this event. Transparent areas within the forest plots  
 333 in Figure 8 represent grid cells that did not have any lidar ground returns (i.e., under dense  
 334 canopy proximal to tree trunks) or were masked due to disturbance (i.e., walking paths in  
 335 clearings). Visual observations on March 13<sup>th</sup> and 14<sup>th</sup> confirmed non-vertical hydrometeor  
 336 trajectories and increased canopy snow loads were observed on the windward side of individual

<sup>337</sup> trees. This effect is shown in Figure 8 to be more apparent in the PWL forest plot than the  
<sup>338</sup> FT forest plot. This may be attributed to the taller trees and higher canopy coverage of the  
<sup>339</sup> PWL forest plot compared to the FT forest plot, as for the same trajectory angle a taller tree  
<sup>340</sup> will produce a larger downwind footprint.

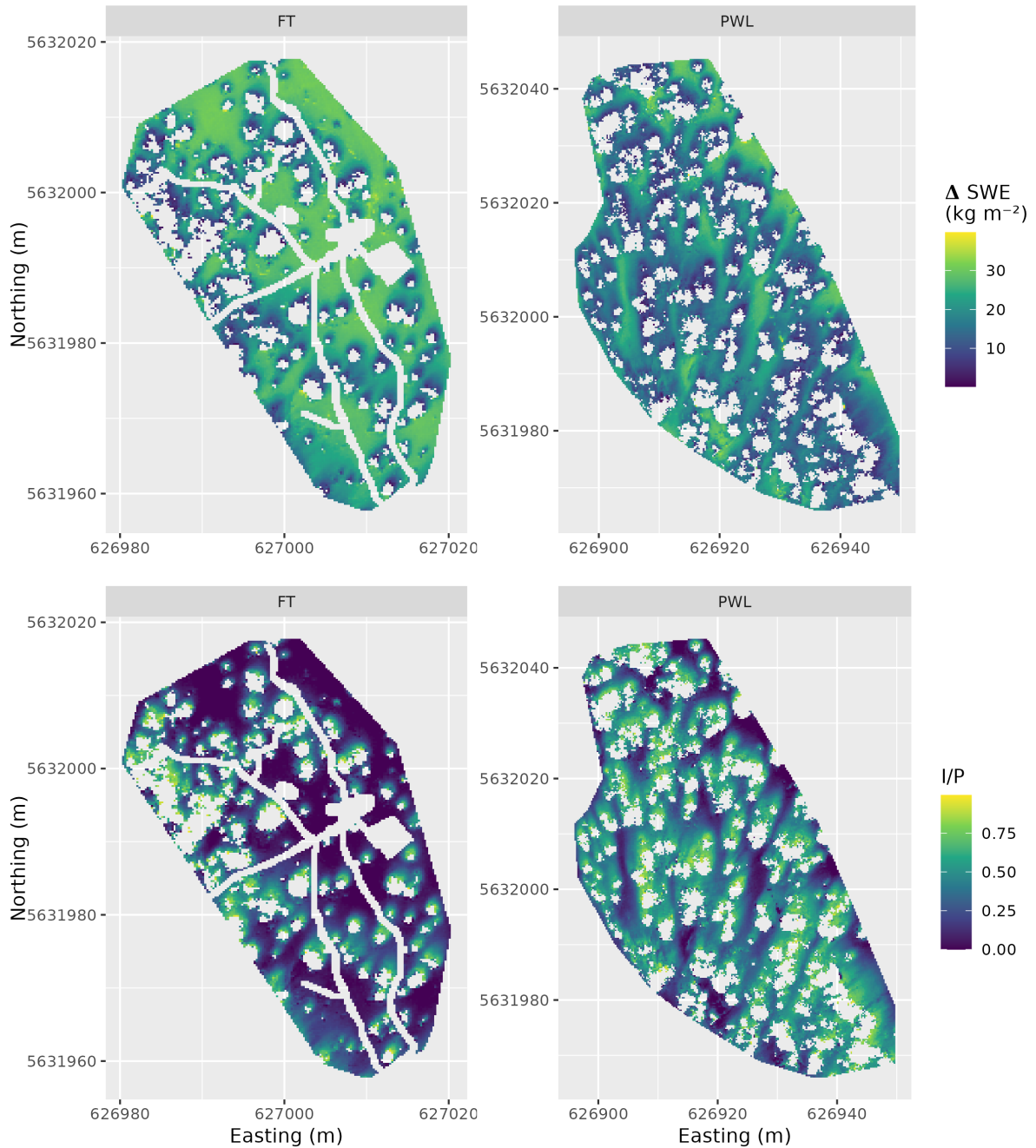


Figure 8: UAV-lidar measurements of the change in snow water equivalent, SWE ( $\text{kg m}^{-2}$ ) and interception efficiency, I/P (-), over the March 13, 2023 24-hour snowfall event for the FT and PWL forest plots at a 0.25 m resolution. See the location of the two forest plots in Figure 1.

Figure 9 shows a strong linear correlation between  $C_p$  and interception efficiency towards the southern portion of the hemisphere, aligning with the average event wind direction. For the PWL forest plot, the upper 97.5<sup>th</sup> percentile of the  $\rho_p$  values shown in Figure 9, were found between azimuth angles of 167°–217°. Similarly, for the FT forest plot, the upper 97.5<sup>th</sup> percentile of  $\rho_p$  was found between azimuth angles of 171°–223°. The zenith angle found to have the highest correlation over this azimuth range was 22° ( $\rho_p = 0.7$ ) and 21° ( $\rho_p = 0.83$ ) for PWL and FT respectively. The high correlation coefficients found for non-vertical zenith angles for both PWL and FT are hypothesized to result from non-vertical hydrometeor trajectories.

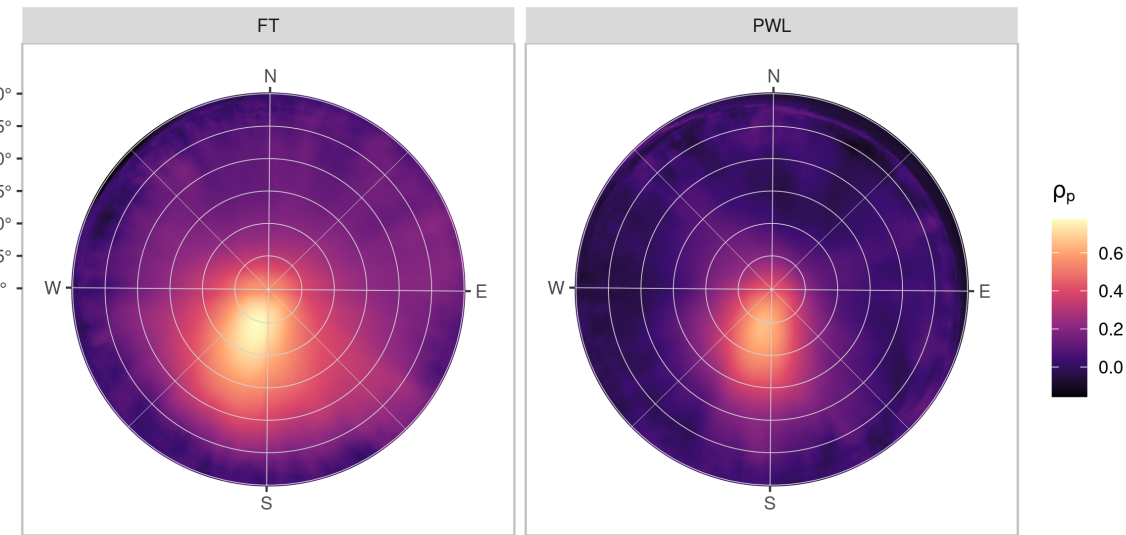


Figure 9: The Pearson Correlation Coefficient between rasters (0.25 m resolution) of interception efficiency and leaf contact area for each grid cell across the study site for each azimuth angles (0°, 1°, ..., 359°) and zenith angles (0°, 1°, ..., 90°) for the FT (left) and PWL (right) forest plots.

The correlation between  $C_p$  and interception efficiency, resampled to a 5 m grid resolution, was higher when  $C_p$  was adjusted for the observed shift in hydrometeor trajectory (Vector Based), compared to the leaf contact angle measured at a zenith angle of 0° (nadir) (Figure 10). The azimuth and zenith angles observed to have the highest  $\rho_p$  in Figure 9 was used to adjust

the vector based,  $C_p$  in Figure 10. The stronger association for the vector-based calculation suggests that adjusted  $C_p$  is a useful predictor of interception efficiency before ablation. An ordinary least squares linear regression forced through the origin was fit to the observed data points using the following equation:

$$\frac{I}{P} = C_p(C_c, \theta_h) \cdot \alpha \quad (9)$$

where  $\alpha$  is an efficiency constant which determines the fraction of snowflakes that contact the  $C_p$  elements and are stored in the canopy (i.e., intercepted) before canopy snow unloading or ablation processes begin.

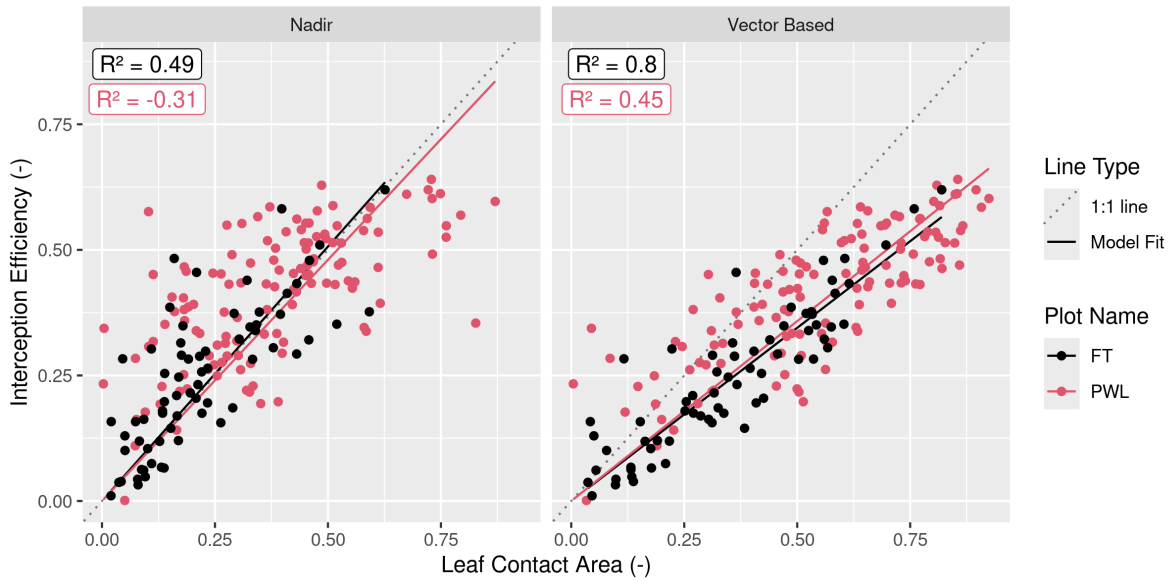


Figure 10: Scatter plots showing the relationship between leaf contact area and interception efficiency rasters resampled to a 5 m grid cell resolution. The left plot (nadir) shows leaf contact area measured from a zenith angle of 0°. The right plot (Vector Based) shows the leaf contact area averaged over rasters with zenith angles (PWL = 22°, FT = 21°) and azimuth angles (PWL = 167°, 178°, ... 217°; FT = 171°, 172°, ... 223°). The solid lines (Model fit) show an ordinary least squares linear regression forced through the origin and fitted to the PWL (red) and FT (black) data and the light grey dotted line shows a 1:1 line. The  $R^2$  values for the four different models are shown in the upper right of each panel calculated following the methods outlined in Kozak & Kozak (1995).

361 For the vector-based model, the relationship between interception efficiency and  $C_p$  results in  
362  $R^2$  values of 0.47 and 0.8 for PWL and FT respectively. The increase in interception efficiency  
363 with  $C_p$  follows a reduced slope compared to the nadir models with  $\alpha$  values of 0.71 and 0.68  
364 for the PWL and FT vector-based models respectively. The reduced slope for the vector-based  
365 models may be due to snowflakes that weaved through and/or bounced off branch elements  
366 in addition to UAV-lidar measurement uncertainty which may have been slightly affected by  
367 unloading and redistribution. These processes would have reduced the fraction of snowfall  
368 that was stored in the canopy. Model error statistics are presented in Table 5 for the nadir  
369 and vector-based models and show the vector-based model provided a better prediction of  
370 interception efficiency. Some of the scatter observed in the nadir model shown in Figure 10  
371 may be explained by grid cells which observed a greater interception efficiency compared to  
372 the corresponding  $C_c$  value and can be attributed to the inability of  $C_c$  to represent the  
373 increase in interception observed within canopy gaps in Figure 8. Conversely, grid cells where  
374 interception efficiency is less than  $C_c$ , may be affected by non-vertical trajectory hydrometeors  
375 making their way underneath the canopy as observed by the reduced interception efficiency  
376 on the windward edges of individual trees in Figure 8. The latter explanation suggests the  
377 non-linear relationship observed for the PWL nadir calculation in Figure 8.

Table 5: Model error statistics provided for predictions of interception efficiency using Equation 9 and for different  $a$  values, as shown in the Model Slope column. Statistics are provided for the PWL and FT forest plots, using leaf contact area canopy metrics adjusted to zenith angles of (0°, 1°, ... 30°) and azimuth angles (170°, 171°, ... 220°) and nadir zenith angle of 0°. The Mean bias is the difference in the model and observed values, MAE is the mean of the absolute error, RMS Error is the root mean squared error,  $R^2$  is the coefficient of determination adjusted using Equation 10 in Kozak & Kozak (1995).

Plot	Canopy	Model Slope	Mean Bias	MAE	RMS Error	
Name	Calculation	(-)	(-)	(-)	(-)	$R^2$
FT	Nadir	0.99	0.022	0.071	0.099	0.51
FT	Vector Based	0.68	0.001	0.047	0.062	0.80
PWL	Nadir	0.95	0.048	0.113	0.146	NA
PWL	Vector Based	0.71	0.019	0.078	0.095	0.47

378    **4.3 The combined influence of trajectory angle and forest structure on  
379    interception**

380    Figure 11 shows that  $C_p$ , measured from VoxRS prior to snowfall on March 13<sup>th</sup>, increases  
381    substantially with simulated hydrometeor trajectory angle and corresponding simulated wind  
382    speed. The standard deviation in VoxRS measured  $C_p$ , illustrated by the shaded area in  
383    Figure 11, exhibits the broad range in values for individual grid cells across each forest plot.  
384    Despite this large scatter, a systematic increase in the mean  $C_p$  across both forest plots results  
385    from a rise in the number of canopy elements for more horizontal angles, when averaged across  
386    each forest plot, over all azimuth angles (see top left panel Figure 11). This results in a large  
387    rise in  $C_p$  over relatively common estimated wind speeds. For example, with a wind speed  
388    of 1 m s<sup>-1</sup> and estimated trajectory angle of 48°,  $C_p$  would increase by 0.31 and 0.28 for the  
389    PWL and FT forest plots respectively (Figure 11). This is a fractional increase in the plot  $C_p$   
390    from nadir of 0.61 and 0.95 for PWL and FT respectively. The increase in  $C_p$  from  $C_c$ , with  
391    increasing trajectory angle is shown on the bottom row of Figure 11 and exhibits a similar

392 relationship for both forest plots FT and PWL until trajectory angles reach approximately  
393  $60^\circ$ . Beyond  $60^\circ$ , the PWL rate of increase slows as the  $C_p$  approaches 1.0, while the FT plot,  
394 which has lower  $C_c$ , continues to rise until around  $75^\circ$  as a  $C_p$  of 1.0 is approached.  $C_p$  was  
395 also quantified across trajectory angles for both PWL and FT on March 14<sup>th</sup>, post snowfall,  
396 and showed a negligible increase in  $C_p$  compared to  $C_p$  measured on March 13<sup>th</sup> without snow  
397 in the canopy.

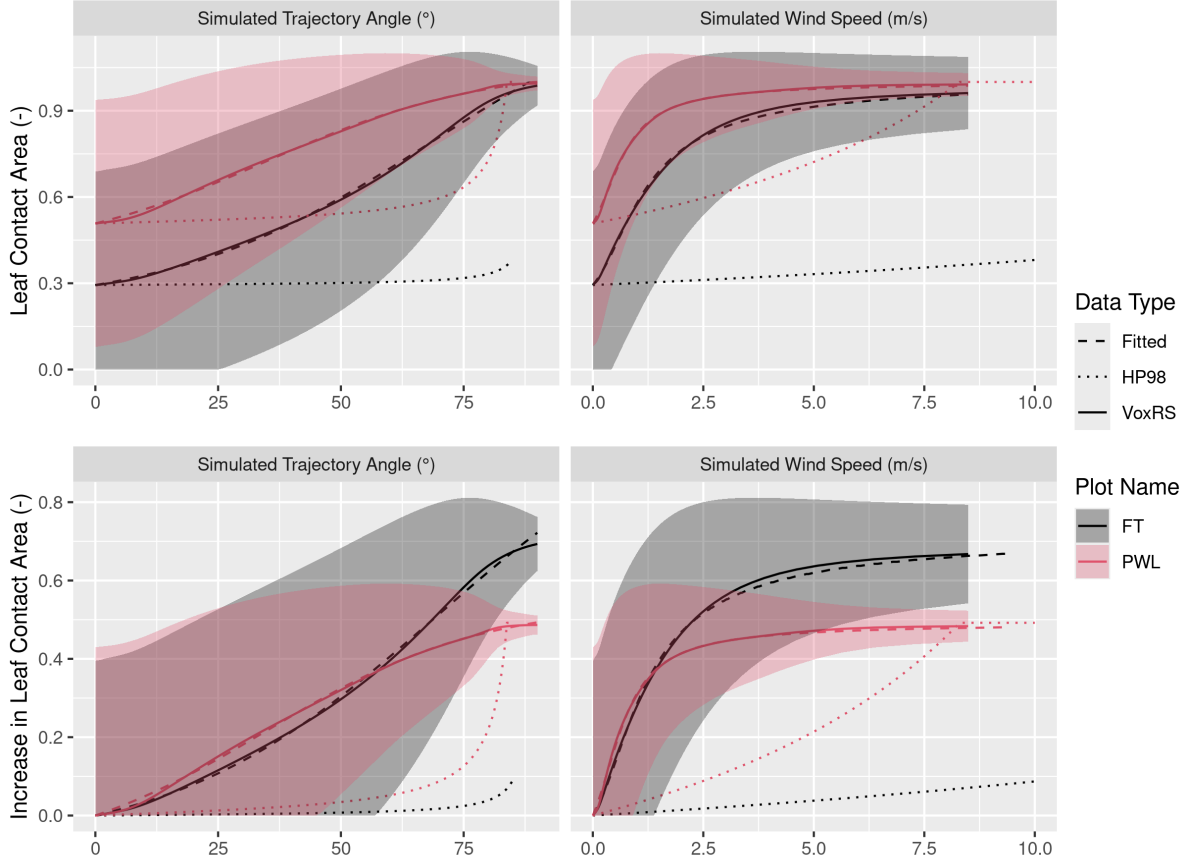


Figure 11: Plots showing the relationship between hydrometeor trajectory angle (left) and wind speed (right) with mean plot-wide snow-leaf contact area,  $C_p$  (top row) and the increase in mean plot-wide  $C_p$ , i.e.,  $C_p - C_c$  (bottom row). The hydrometeor trajectory angle is simulated through VoxRS and is measured as degrees from zenith. Simulated wind speed was calculated as a function of hydrometeor trajectory angle by rearranging Equation 4 and an observed event hydrometeor velocity of 0.9 m s<sup>-1</sup>. The solid lines (VoxRS) represent the mean  $C_p$  (top row) or increase in mean  $C_p$  (bottom row) for a single zenith angle observed from VoxRS across all grid cells for each forest plot and across all azimuth angles. The shaded area represents 1 standard deviation above and below the observed VoxRS mean. The dashed lines (Fitted) represent predictions from Equation 10 (top) and Equation 11 (bottom). The dotted lines (HP98) represent the predictions from Equation 10 in Hedstrom & Pomeroy (1998). A forested downwind distance of 100 m was assumed for the HP98 calculation.

398 A function is proposed here to calculate plot scale leaf contact area,  $C_p$  (-):

$$C_p = C_c + C_{inc}(\theta_h) \quad (10)$$

399 where,  $C_{inc}$  is the increase in leaf contact area from  $C_c$  which is a function of  $\theta_h$ . To estimate  
 400  $C_{inc}$  a non-linear least squares regression using a logistic function forced through the origin was  
 401 fit to the VoxRS measurements at FT and PWL for simulated hydrometeor trajectory angles  
 402 (see dashed lines in bottom row of Figure 11). A logistic function was selected to model this  
 403 relationship, as its shape reflects the slow increase in observed  $C_p$  at near vertical trajectory  
 404 angles, followed by a rapid increase to represent increase canopy area in the middle and lower  
 405 section of individual trees, and the gradual leveling off as  $C_p$  approaches a value of 1.0. The  
 406 logistic function used to predict  $C_{inc}$  as a function of  $\theta_h$  is:

$$C_{inc} = \left( \frac{C_{inc}^{max}}{1 + e^{\left(\frac{\theta_0 - \theta_h}{k}\right)}} - \frac{C_{inc}^{max}}{1 + e^{\left(\frac{\theta_0}{k}\right)}} \right) \quad (11)$$

407 where  $C_{inc}^{max}$  is the maximum value of  $C_{inc}$ ,  $\theta_0$  is the x-value of the sigmoid midpoint and  $k$  is the  
 408 logistic growth rate or steepness of the curve. The coefficients resulting from the non-linear  
 409 least squares regression fit of Equation 11 to the VoxRS dataset are presented in Table 6.  
 410 Simulated  $C_p$  using Equation 10 is shown in the dashed lines in the top row of Figure 11  
 411 and follows the VoxRS-measured mean  $C_p$  closely. Model error statistics shown in Table 7  
 412 demonstrate that Equation 11 performed well, with a mean bias and RMSE of 0.001 (-) and  
 413 0.0054 (-) respectively for PWL, and -0.0004 (-) and 0.0079 (-) for FT. In contrast, Table 7  
 414 reveals that the Hedstrom & Pomeroy (1998) method produced significantly less accurate  
 415 estimates of  $C_p$ , with a mean bias and RMSE of -0.201 (-) and 0.233 (-) respectively for PWL,  
 416 and -0.260 (-) and 0.324 (-) for FT.

Table 6: Coefficients derived from the non-linear least squares regression fit of Equation 11 to the VoxRS dataset.

Plot Names	$C_{inc}^{max}$	$\theta_0$	$k$
PWL	0.66	34.58	22.14
FT	1.18	69.13	26.98

Table 7: Model error statistics calculated for the prediction of leaf contact area from trajectory angle using Equation 11 (nls) and Equation 10 from Hedstrom & Pomeroy (1998) for the PWL and FT forest plots. Mean bias is the difference in the model and observed values, MAE is the mean of the absolute error, RMS Error is the root mean squared error and  $R^2$  is the coefficient of determination. The units for all metrics are dimensionless. A forested downwind distance of 100 m was used for the HP98 calculation.

Model	Plot Name	Mean Bias (-)	MAE (-)	RMS Error (-)	$R^2$
HP98	FT	-0.26	0.26	0.32	0.72
HP98	PWL	-0.20	0.20	0.23	0.44
nls	FT	0.00	0.01	0.01	1.00
nls	PWL	0.00	0.00	0.01	1.00

#### 417 4.4 Throughfall model performance

418 The performance of Equations 9, 10, and 11 in estimating event throughfall was assessed  
 419 against UAV-lidar measurements of throughfall for the March 13–14<sup>th</sup> snowfall event at the  
 420 plot scale for both FT and PWL. Required values for the model included the event mean  
 421 hydrometeor terminal velocity and event total snowfall which were measured at PWL station,  
 422 and wind speed was taken as one-third the mean canopy height using the wind speed profile in  
 423 Figure 7. Additional model inputs include the mean  $C_c$  for each plot which was measured from  
 424 the VoxRS dataset. An  $\alpha$  value of 0.836 (-) was found through calibration which provided the

<sup>425</sup> best fit between observed and simulated interception efficiency at the plot scale for both FT  
<sup>426</sup> and PWL.

<sup>427</sup> Figure 12 shows the vector-based model, computed using Equation 9 with  $C_p$  adjusted for esti-  
<sup>428</sup> mated hydrometeor trajectory angle, closely matches UAV-lidar measurements of throughfall.  
<sup>429</sup> Observed and modelled values of interception efficiency and  $\Delta SWE_{tf}$  are presented in Table 8  
<sup>430</sup> along with corresponding error statistics. Modelled throughfall from the vector-based model  
<sup>431</sup> was 17 kg m<sup>-2</sup> compared to the measured throughfall of 16.6 kg m<sup>-2</sup> for PWL. For FT, the  
<sup>432</sup> vector-based modelled throughfall was 21.8 kg m<sup>-2</sup>, while the measured values were 22.1 kg  
<sup>433</sup> m<sup>-2</sup>. The vector-based model shows a lower mean bias of -0.3 kg m<sup>-2</sup> for PWL and a negative  
<sup>434</sup> bias of 0.3 kg m<sup>-2</sup> for FT, compared to the larger mean bias of -1.6 kg m<sup>-2</sup> for PWL and -0.8  
<sup>435</sup> kg m<sup>-2</sup> for FT with the nadir-model (calculated using  $C_c$  in place of  $C_p$ ). This resulted in a  
<sup>436</sup> large reduction in the percent error in predicted throughfall, from -9.4% with the nadir-model  
<sup>437</sup> to -1.8% with the vector-based model for PWL. A smaller improvement was observed for FT,  
<sup>438</sup> with the percent error in predicted throughfall declining from -3.6% with the nadir-model to  
<sup>439</sup> -1.4% with the vector-based model.

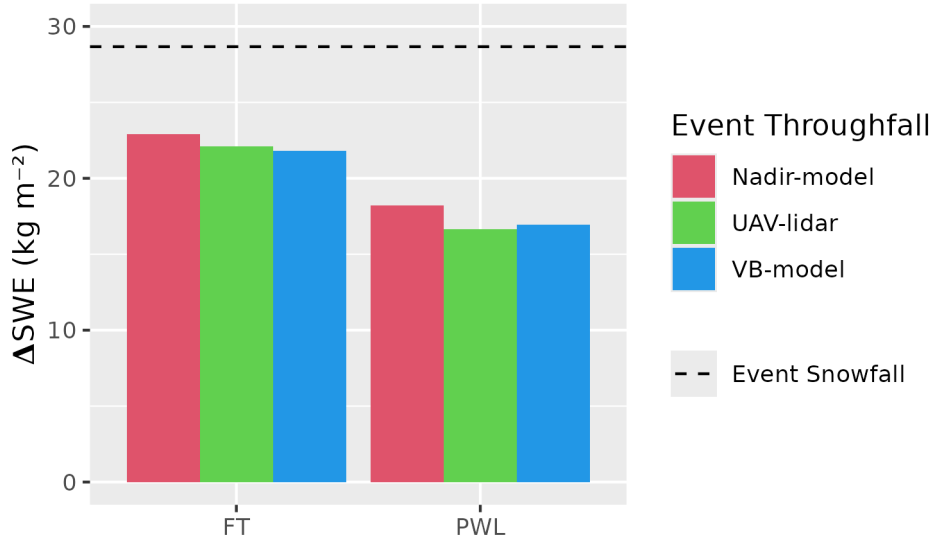


Figure 12: Bar chart comparing the observed and modelled mean change in throughfall ( $\Delta\text{SWE}$ ,  $\text{kg m}^{-2}$ ) over the March 13-14 snowfall event averaged over forest plots FT and PWL. The ‘Nadir-model’ used Equation 9 not adjusted for trajectory angle (i.e.,  $C_c$ ) and the Vector-based ‘VB-model’ which uses Equation 9 with  $C_p$  adjusted for trajectory angle. ‘UAV-lidar’ corresponds to throughfall calculated using Equation 6 incorporating UAV-lidar snow depth and snow density from in-situ snow pits. The black horizontal dashed line shows the accumulated SWE ( $\text{kg m}^{-2}$ ) over the snowfall event to the PWL station open clearing.

Table 8: Model error statistics for model estimates of snow interception efficiency (I/P) and throughfall (TF) compared to measurements of I/P and TF using UAV-lidar averaged over the FT and PWL forest plots. Units for I/P are (-) and TF are ( $\text{kg m}^{-2}$ ). The vector-based model utilized Equation 9 with  $C_p$  adjusted for trajectory angle. The nadir model also utilized Equation 9 but was not adjusted for trajectory angle and thus  $C_c$  was used instead of  $C_p$ . The ‘Obs. Value’ column contains measurements from UAV-lidar while the ‘Mod. Value’ column contains the modelled values. The mean bias was calculated as observed minus modelled and percent error is the percent error between predicted and observed values.

Plot	Model	Value		Obs.	Mod.	Mean	Perc.
Plot	Type	Name	Units	Value	Value	Bias	Error
FT	VB-	I/P	-	0.23	0.24	-0.01	-4.67
	model						
FT	Nadir-	I/P	-	0.23	0.20	0.03	12.10
	model						
FT	VB-	TF	$\text{kg m}^{-2}$	22.12	21.82	0.31	1.38
	model						
FT	Nadir-	TF	$\text{kg m}^{-2}$	22.12	22.91	-0.79	-3.58
	model						
PWL	VB-	I/P	-	0.42	0.41	0.01	2.54
	model						
PWL	Nadir-	I/P	-	0.42	0.37	0.05	12.95
	model						
PWL	VB-	TF	$\text{kg m}^{-2}$	16.64	16.95	-0.31	-1.84
	model						
PWL	Nadir-	TF	$\text{kg m}^{-2}$	16.64	18.20	-1.56	-9.35
	model						

<sup>440</sup> **5 Discussion**

<sup>441</sup> The point scale observations presented in Figure 6 show air temperature had little influence  
<sup>442</sup> on interception efficiency. This differs from existing studies which suggested either a positive  
<sup>443</sup> (Storck et al., 2002) or negative (Hedstrom & Pomeroy, 1998) relationship. A weak relationship,  
<sup>444</sup> that leaves 80–90% of variance unexplained, was observed between initial interception efficiency  
<sup>445</sup> (before unloading) with increasing wind speed at two locations which were sheltered from the  
<sup>446</sup> predominant wind direction (Figure 6b). This is attributed to an associated increase in  $C_p$   
<sup>447</sup> due to non-vertical hydrometeor trajectories. These results are consistent with observations  
<sup>448</sup> by Schmidt & Troendle (1989) who observed a slight increase in snowfall interception with  
<sup>449</sup> increasing wind speeds up to  $6 \text{ m s}^{-1}$  and studies of rainfall interception by Herwitz & Slye  
<sup>450</sup> (1995) and Van Stan et al. (2011).

<sup>451</sup> Compared to the influence of wind speed, interception efficiency showed a smaller sensitivity  
<sup>452</sup> to canopy snow load at the point scale (Figure 5). The slight increase in interception efficiency  
<sup>453</sup> for smaller canopy snow loads and decline for larger canopy snow loads is attributed to the  
<sup>454</sup> influence of canopy snow load on  $C_p$  (Figure 6c). While small, this effect is consistent with  
<sup>455</sup> the theory proposed by Satterlund & Haupt (1967) that interception efficiency increases as  
<sup>456</sup> the canopy fills with snow bridging gaps in the canopy increasing, while later declining due to  
<sup>457</sup> branch bending and decreased canopy coverage. However, the observations shown in Figure 6  
<sup>458</sup> and Figure 3, which minimized ablation processes, differ from those reported by Satterlund  
<sup>459</sup> & Haupt (1967), Schmidt & Pomeroy (1990), and Moeser et al. (2015), as canopy snow load  
<sup>460</sup> increased linearly with snowfalls up to  $45 \text{ kg m}^{-2}$  without approaching a maximum canopy snow  
<sup>461</sup> load. The strong decline in interception efficiency with increasing event snowfall in Satterlund  
<sup>462</sup> & Haupt (1967) and Schmidt & Pomeroy (1990) may have resulted from higher unloading rates  
<sup>463</sup> as branches bent under heavy snow loads, hence mixing ablation and interception processes to  
<sup>464</sup> varying degrees. In contrast, other studies (Calder, 1990; Lundquist et al., 2021; Watanabe &  
<sup>465</sup> Ozeki, 1964) align with the observations in Figure 6 and Figure 3, showing little evidence of  
<sup>466</sup> a reduced interception efficiency with increasing snowfall. The low sensitivity of interception

efficiency with canopy snow load found in this study and others may be attributed to several factors: a reduced inclusion of ablation processes in the interception efficiency measurements, limited influence of canopy snow load on  $C_p$  at this study site, and/or the compensatory effects outlined by Satterlund & Haupt (1967).

Staines & Pomeroy (2023) showed a slight increase in VoxRS measured  $C_p$  between snow-off and snow-on conditions. However, the increase in  $C_p$  resulting from snow load in Staines & Pomeroy (2023) was small compared to the substantial rise in  $C_p$  due to trajectory angle presented in their study and as shown in Figure 11. Both findings from Staines & Pomeroy (2023) corroborate the results reported in this study. Further evidence in support of the relatively small influence of canopy snow load on  $C_p$ , is provided by Lundquist et al. (2021) who reported improved simulation of subcanopy snow accumulation without the use of a maximum canopy snow load, when linked with a comprehensive canopy snow ablation routine. Lehtonen et al. (2016) also note that in northern Finland heavy canopy snow loads have been observed to continue increasing until stem breakage, under conditions favourable for the formation of significant rime-ice accretion and limited ablation, thus reducing  $C_p$ . Models are available to predict the accretion of ice on tree canopies (e.g., Nock et al., 2016) however, further research is required to understand the canopy snow load required to cause stem breakage across different tree species and canopy loads.

These findings on the limited influence of air temperature and canopy snow load on initial interception challenge the theoretical basis of many existing snow interception parameterizations (Hedstrom & Pomeroy, 1998; Moeser et al., 2015; Satterlund & Haupt, 1967; Storck et al., 2002). To address this, a new snow interception parameterization, introduced in Equation 9, is presented which calculates interception efficiency as a function of  $C_p$  and  $\alpha$ . This new parameterization allows for canopy snow loading processes to be isolated from canopy snow ablation processes and is consistent with current rainfall interception theory (Valante et al., 1997). Equation 9 differs only slightly from the original Hedstrom & Pomeroy (1998) parameterization (see Equation 6 in Hedstrom & Pomeroy 1998), in that it does not calculate interception efficiency as a function of canopy snow load and from the Storck et al. (2002)

parameterization who found interception efficiency to be constant. The theoretical basis of the  $\alpha$  parameter in Equation 9 is that the association between  $C_p$  and interception efficiency, as shown in Figure 10, unlike existing rainfall parameterizations (Valante et al., 1997) does not follow a 1:1 line, as falling snow hydrometeors may bounce off the canopy elements. Further research is needed to explore how processes such as the increased cohesion and adhesion of snowfall to the canopy at warm temperatures, as observed by Kobayashi (1987), Pfister & Schneebeli (1999), Storck et al. (2002), as well as hydrometeor velocity, particle size, and shape suggested by (Katsushima et al., 2023), may influence the  $\alpha$  parameter, although these effects were not observed in this study.

Measurements of interception efficiency and canopy structure, as shown in Figure 8, align with the theory proposed by Hedstrom & Pomeroy (1998) which suggests reduced throughfall on the lee side of individual trees for a wind driven snowfall event. However, an existing exponential relationship proposed in Hedstrom & Pomeroy (1998) to scale canopy coverage with wind speed failed to reproduce the observations presented in Figure 11. Instead, plot-wide  $C_{inc}$  was found to increase as logistic function of  $\theta_h$  and  $C_c$ . Significant scatter in VoxRS measured  $C_p$  across the two forest plots, illustrated by the high standard deviation in Figure 11, resulted from directional (azimuth) and spatial differences in canopy structure. This large scatter suggests the observed relationships in Figure 11 are only applicable at the forest stand scale where the sub-metre variability in  $C_p$  averages out. For example, at the point scale, the mixed canopy SCL which is open to the prevailing wind direction (Figure 2), had an increase in throughfall with increasing wind speed (Figure 5 & Figure 6). However, Figure 11 shows that at the plot scale,  $C_p$  rises with increasing  $\theta_h$ , as there is a greater number of grid cells which have more closed canopy at more horizontal angles. Still, Equation 11 would not be applicable to areas that have large continuous gap fractions (e.g., large forested clear cuts) that are many times wider than the mean canopy height. Staines & Pomeroy (2023) have also shown that backflows and large eddies that occur within the canopy can also contribute to mixed responses. Further work is required to refine the relationship proposed in Equation 11 across a range of tree species and densities.

523 It was found that the mean event hydrometeor trajectory angle, required for Equation 11, could  
524 be predicted from Equation 4 using the observed mean hydrometeor fall velocity and the mean  
525 horizontal wind speed selected at one-third of the canopy height above the ground. A wind  
526 speed at one-third the mean canopy height is hypothesized to be important for canopy snow  
527 accumulation as a large fraction of the horizontal cross-sectional area is at this height for most  
528 needleleaf canopies. Katsushima et al. (2023), also proposed the wind speed at one-third the  
529 canopy height for modelling unloading of canopy snow as it corresponds to the centre of gravity  
530 when the horizontal projection of the canopy is assumed to be a triangle. However, there is  
531 uncertainty in the transferability of the canopy height observed here to other environments  
532 due to differing tree structures and tree species. This may include forests with a larger trunk  
533 space or have more of their canopy contact area at higher heights above the ground (i.e., some  
534 deciduous canopies). Moreover, Equation 4 assumes a linear hydrometeor trajectory, and does  
535 not consider non-linear patterns such as wind flow directions around tree elements, turbulent  
536 flow, or differences in wind speed with height.

537 Although the improvement in performance of the vector-based model over the nadir model was  
538 relatively small, the vector-based model is preferred due to its overall lower error compared  
539 to the UAV-lidar measurements and better representation of physical processes. While the  
540 vector-based model acts to increase interception efficiency with wind speed, several studies  
541 have shown that canopy snow ablation increases as a result of wind induced unloading (Bartlett  
542 & Verseghy, 2015; Betts & Ball, 1997; Lumbrago et al., 2022; Roesch et al., 2001; Wheeler,  
543 1987). Thus, representing both the increase in initial interception due to inclined hydrometeor  
544 trajectory angles and the subsequent increase in canopy snow unloading will be important in  
545 subcanopy snow accumulation models.

## 546 **6 Conclusions**

547 New observations of initial snow interception, collected over a wide range of meteorological  
548 conditions and canopy structures indicate that forest structure is the primary factor influencing

549 subcanopy snow accumulation. At the point scale, high-temporal resolution measurements  
550 revealed no evidence of a maximum canopy snow load, even for event snowfalls up to 45 kg  
551  $m^{-2}$ , nor was there any indication of air temperature influencing the cohesion and adhesion of  
552 snowfall to the canopy or branch bending reducing canopy coverage. Instead, wind speed was  
553 found to influence interception efficiency by changing the hydrometeor trajectory angle, which  
554 can lead to a substantial increase in snow-leaf contact area.

555 At the forest plot scale, UAV-lidar measurements of throughfall aligned with the point-scale  
556 observations demonstrating that leaf contact area was the primary factor influencing inter-  
557ception efficiency at a particular site. Leaf contact area, which incorporates changes in the  
558 number of canopy contacts with hydrometeor trajectory angle, proved to be a better predic-  
559 tor of interception efficiency compared to nadir-calculated canopy coverage. When averaged  
560 across each forest plot, leaf contact area was shown to be highly sensitive to trajectory angle,  
561 increasing by 61–95% for trajectory angles associated with a  $1\text{ m s}^{-1}$  wind speed. An existing  
562 theoretical relationship failed to adequately represent the VoxRS-measured increase in leaf  
563 contact area with simulated trajectory angles. As a result, a new relationship is proposed,  
564 which demonstrated good performance at this study site.

565 The weak association between air temperature and canopy snow load with interception effi-  
566 ciency, as presented here and in other recent studies, coupled with the influence of wind speed  
567 on leaf contact area, highlights the need for a new snow interception parameterization. A new  
568 parameterization is proposed that calculates initial interception as a function of snowfall and  
569 leaf contact area. This parameterization is consistent with rainfall interception studies, which  
570 also separate canopy loading and ablation processes, and calculate interception as a function  
571 of canopy coverage. Additionally, a second equation is proposed to estimate leaf contact area  
572 as a function of hydrometeor trajectory angle and nadir canopy coverage. This updated snow  
573 interception parameterization performed well in the subalpine forest studied here. However,  
574 further validation is necessary in a range of climates, forest species, and canopy structures.

<sup>575</sup> **7 Acknowledgments**

<sup>576</sup> We wish to acknowledge financial support from the University of Saskatchewan Dean's Schol-  
<sup>577</sup> arship, Natural Sciences and Engineering Research Council of Canada, Global Water Futures  
<sup>578</sup> Programme, Environment and Climate Change Canada, Alberta Innovates, Canada Founda-  
<sup>579</sup> tion for Innovation, and the Canada Research Chairs Programme. We thank Madison Harasyn,  
<sup>580</sup> Hannah Koslowsky, Kieran Lehan, Lindsey Langs and Fortress Mountain Resort for their help  
<sup>581</sup> in the field. Jacob Staines, Madison Harasyn, Alistair Wallace, and Rob White contributed  
<sup>582</sup> to developing the UAV-lidar processing workflow.

<sup>583</sup> **8 Data Availability**

<sup>584</sup> The data that support the findings in this study are available at <https://doi.org/10.5281/zenodo.14018893>.

585    **References**

- 586    Bartlett, P. A., & Verseghy, D. L. (2015). Modified treatment of intercepted snow improves  
587    the simulated forest albedo in the Canadian Land Surface Scheme. *Hydrological Processes*,  
588    29(14), 3208–3226. <https://doi.org/10.1002/HYP.10431>
- 589    BayesMap Solutions. (2024). *BayesStripAlign*. <https://bayesmap.com/products/bayesstripalign/>
- 590    Betts, A. K., & Ball, J. H. (1997). Albedo over the boreal forest. *Journal of Geophysical  
591    Research: Atmospheres*, 102(D24), 28901–28909. [https://doi.org/https://doi.org/10.1029/96JD03876](https://doi.org/10.1029/96JD03876)
- 592    Calder, I. R. (1990). *Evaporation in the uplands* (p. 148). Wiley.
- 593    Cebulski, A., & Pomeroy, J. W. (2024). The theoretical underpinnings of snow interception  
594    and ablation parameterizations. *Wiley Interdisciplinary Reviews: Water, In Review*.
- 595    Chianucci, F., & Macek, M. (2023). hemispheR: an R package for fisheye canopy image  
596    analysis. *Agricultural and Forest Meteorology*. <https://doi.org/10.1016/j.agrformet.2023.109470>
- 597    Cionco, R. M. (1965). A Mathematical Model for Air Flow in a Vegetative Canopy. *Journal of  
598    Applied Meteorology* (1962), 4(4), 517–522. [https://doi.org/https://doi.org/10.1175/1520-0450\(1965\)004%3C0517:AMMFAF%3E2.0.CO;2](https://doi.org/https://doi.org/10.1175/1520-0450(1965)004%3C0517:AMMFAF%3E2.0.CO;2)
- 599    Ellis, C. R., Pomeroy, J. W., & Link, T. E. (2013). Modeling increases in snowmelt yield and  
600    desynchronization resulting from forest gap-thinning treatments in a northern mountain  
601    headwater basin. *Water Resources Research*, 49(2), 936–949. <https://doi.org/10.1002/wrcr.20089>
- 602    Essery, R., Pomeroy, J. W., Parviainen, J., & Storck, P. (2003). Sublimation of snow from  
603    coniferous forests in a climate model. *Journal of Climate*, 16(11), 1855–1864. [https://doi.org/10.1175/1520-0442\(2003\)016%3C1855:SOSFCF%3E2.0.CO;2](https://doi.org/10.1175/1520-0442(2003)016%3C1855:SOSFCF%3E2.0.CO;2)
- 604    Fryer, B. Y. G. I., Johnson, E. A., Fryer, G. I., & Johnson, E. A. (1988). Reconstructing  
605    Fire Behaviour and Effects in a Subalpine Forest. *The Journal of Applied Ecology*, 25(3),  
606    1063–1072. <https://doi.org/https://doi.org/10.2307/2403766>

- 613 Gelfan, A. N., Pomeroy, J. W., & Kuchment, L. S. (2004). Modeling forest cover influences on  
614 snow accumulation, sublimation, and melt. *Journal of Hydrometeorology*, 5(5), 785–803.  
615 [https://doi.org/10.1175/1525-7541\(2004\)005%3C0785:MFCIOS%3E2.0.CO;2](https://doi.org/10.1175/1525-7541(2004)005%3C0785:MFCIOS%3E2.0.CO;2)
- 616 Golding, D. L., & Swanson, R. H. (1978). Snow accumulation and melt in small forest openings  
617 in Alberta. *Canadian Journal of Forest Research*, 8(4), 380–388. <https://doi.org/https://doi.org/10.1139/x78-057>
- 619 Harder, P., & Pomeroy, J. W. (2013). Estimating precipitation phase using a psychrometric  
620 energy balance method. *Hydrological Processes*, 27(13), 1901–1914. <https://doi.org/https://doi.org/10.1002/hyp.9799>
- 622 Harder, P., Pomeroy, J. W., & Helgason, W. D. (2020). Improving sub-canopy snow depth  
623 mapping with unmanned aerial vehicles: Lidar versus structure-from-motion techniques.  
624 *Cryosphere*, 14(6), 1919–1935. <https://doi.org/10.5194/tc-14-1919-2020>
- 625 Harpold, A. A., Krogh, S. A., Kohler, M., Eckberg, D., Greenberg, J., Sterle, G., & Broxton,  
626 P. D. (2020). Increasing the efficacy of forest thinning for snow using high-resolution  
627 modeling: A proof of concept in the Lake Tahoe Basin, California, USA. *Ecohydrology*,  
628 13(4). <https://doi.org/10.1002/eco.2203>
- 629 Hedstrom, N. R., & Pomeroy, J. W. (1998). Measurements and modelling of snow interception  
630 in the boreal forest. *Hydrological Processes*, 12(10-11), 1611–1625. [https://doi.org/10.1002/\(SICI\)1099-1085\(199808/09\)12:10/11%3C1611::AID-HYP684%3E3.0.CO;2-4](https://doi.org/10.1002/(SICI)1099-1085(199808/09)12:10/11%3C1611::AID-HYP684%3E3.0.CO;2-4)
- 632 Herwitz, S. R., & Slye, R. E. (1995). Three-dimensional modeling of canopy tree interception  
633 of wind-driven rainfall. *Journal of Hydrology*, 168(1-4), 205–226. [https://doi.org/10.1016/0022-1694\(94\)02643-P](https://doi.org/10.1016/0022-1694(94)02643-P)
- 635 Hijmans, R. J. (2024). *terra: Spatial Data Analysis*. <https://cran.r-project.org/package=terra>
- 636 Katsushima, T., Kato, A., Aiura, H., Nanko, K., Suzuki, S., Takeuchi, Y., & Murakami, S.  
637 (2023). Modelling of snow interception on a Japanese cedar canopy based on weighing  
638 tree experiment in a warm winter region. *Hydrological Processes*, 37(6), 1–16. <https://doi.org/10.1002/hyp.14922>
- 640 Kim, E., Gatebe, C., Hall, D., Newlin, J., Misakonis, A., Elder, K., Marshall, H. P., Hiem-  
641 stra, C., Brucker, L., De Marco, E., Crawford, C., Kang, D. H., & Entin, J. (2017).

- 642 NASA's snowex campaign: Observing seasonal snow in a forested environment. *2017*  
643 *IEEE International Geoscience and Remote Sensing Symposium (IGARSS)*, 1388–1390.  
644 <https://doi.org/10.1109/IGARSS.2017.8127222>
- 645 Kobayashi, D. (1987). Snow accumulation on a narrow board. *Cold Regions Science and*  
646 *Technology*, *13*(3), 239–245. [https://doi.org/https://doi.org/10.1016/0165-232X\(87\)90005-X](https://doi.org/10.1016/0165-232X(87)90005-X)
- 648 Kozak, A., & Kozak, R. A. (1995). Notes on regression through the origin. *Forestry Chronicle*,  
649 *71*(3), 326–330. [https://doi.org/https://doi.org/10.5558/tfc71326-3](https://doi.org/10.5558/tfc71326-3)
- 650 Langs, L. E., Petrone, R. M., & Pomeroy, J. W. (2020). A  $\delta^{18}\text{O}$  and  $\delta^2\text{H}$  stable water  
651 isotope analysis of subalpine forest water sources under seasonal and hydrological stress  
652 in the Canadian Rocky Mountains. *Hydrological Processes*, *34*(26), 5642–5658. <https://doi.org/10.1002/hyp.13986>
- 654 LAStools. (2024). *Efficient LiDAR Processing Software (version 240220, academic)*. <http://rapidlasso.com/LAStools>
- 656 Lehtonen, I., Kämärainen, M., Gregow, H., Venäläinen, A., & Peltola, H. (2016). Heavy snow  
657 loads in Finnish forests respond regionally asymmetrically to projected climate change.  
658 *Natural Hazards and Earth System Sciences*, *16*(10), 2259–2271. <https://doi.org/10.5194/nhess-16-2259-2016>
- 660 Lumbrazo, C., Bennett, A., Currier, W. R., Nijssen, B., & Lundquist, J. (2022). Evaluating  
661 Multiple Canopy-Snow Unloading Parameterizations in SUMMA With Time-Lapse  
662 Photography Characterized by Citizen Scientists. *Water Resources Research*, *58*(6), 1–22.  
663 <https://doi.org/10.1029/2021WR030852>
- 664 Lundberg, A., & Hallidin, S. (1994). Evaporation of intercepted snow: Analysis of governing  
665 factors. *Water Resources Research*, *30*(9), 2587–2598. <https://doi.org/10.1029/94WR00873>
- 667 Lundquist, J. D., Dickerson-Lange, S., Gutmann, E., Jonas, T., Lumbrazo, C., & Reynolds, D.  
668 (2021). Snow interception modelling: Isolated observations have led to many land surface  
669 models lacking appropriate temperature sensitivities. *Hydrological Processes*, *35*(7), 1–20.  
670 <https://doi.org/10.1002/hyp.14274>

- 671 MacDonald, J. P. J. (2010). *Unloading of intercepted snow in conifer forests* (Master of  
672 Science August, University of Saskatchewan; pp. 0–93). <http://hdl.handle.net/10388/etd-09302010-145706>
- 673
- 674 Moeser, D., Stähli, M., & Jonas, T. (2015). Improved snow interception modeling using  
675 canopy parameters derived from airborne LiDAR data. *Water Resources Research*, 51(7),  
676 5041–5059. <https://doi.org/https://doi.org/10.1002/2014WR016724>
- 677 Musselman, K. N., Pomeroy, J. W., & Link, T. E. (2015). Variability in shortwave irradiance  
678 caused by forest gaps: Measurements, modelling, and implications for snow energetics.  
679 *Agricultural and Forest Meteorology*, 207, 69–82. <https://doi.org/https://doi.org/10.1016/j.agrformet.2015.03.014>
- 680
- 681 Nock, C. A., Lecigne, B., Taugourdeau, O., Greene, D. F., Dauzat, J., Delagrange, S.,  
682 & Messier, C. (2016). Linking ice accretion and crown structure: towards a model  
683 of the effect of freezing rain on tree canopies. *Annals of Botany*, 117(7), 1163–1173.  
684 <https://doi.org/https://doi.org/10.1093/aob/mcw059>
- 685 Pfister, R., & Schneebeli, M. (1999). Snow accumulation on boards of different sizes and  
686 shapes. *Hydrological Processes*, 13(14–15), 2345–2355. [https://doi.org/https://doi.org/10.1002/\(SICI\)1099-1085\(199910\)13:14/15%3C2345::AID-HYP873%3E3.0.CO;2-N](https://doi.org/https://doi.org/10.1002/(SICI)1099-1085(199910)13:14/15%3C2345::AID-HYP873%3E3.0.CO;2-N)
- 687
- 688 Pomeroy, J. W., Brown, T., Fang, X., Shook, K. R., Pradhananga, D., Armstrong, R., Harder,  
689 P., Marsh, C., Costa, D., Krogh, S. A., Aubry-wake, C., Annand, H., Lawford, P., He,  
690 Z., Kompanizare, M., & Moreno, J. I. L. (2022). The cold regions hydrological modelling  
691 platform for hydrological diagnosis and prediction based on process understanding. *Journal  
692 of Hydrology*, 615(128711), 1–25. <https://doi.org/10.1016/j.jhydrol.2022.128711>
- 693
- 694 Pomeroy, J. W., Fang, X., & Ellis, C. R. (2012). Sensitivity of snowmelt hydrology in Marmot  
695 Creek, Alberta, to forest cover disturbance. *Hydrological Processes*, 26(12), 1891–1904.  
<https://doi.org/10.1002/hyp.9248>
- 696
- 697 Pomeroy, J. W., Marsh, P., & Gray, D. M. (1997). Application of a distributed blowing snow  
698 model to the arctic. *Hydrological Processes*, 11(11), 1451–1464. [https://doi.org/10.1002/\(sici\)1099-1085\(199709\)11:11%3C1451::aid-hyp449%3E3.0.co;2-q](https://doi.org/10.1002/(sici)1099-1085(199709)11:11%3C1451::aid-hyp449%3E3.0.co;2-q)
- 699 Pomeroy, J. W., Parviainen, J., Hedstrom, N., & Gray, D. M. (1998). Coupled modelling of

- 700 forest snow interception and sublimation. *Hydrological Processes*, 12(15), 2317–2337. [https://doi.org/10.1002/\(SICI\)1099-1085\(199812\)12:15%3C2317::AID-HYP799%3E3.0.CO;2-X](https://doi.org/10.1002/(SICI)1099-1085(199812)12:15%3C2317::AID-HYP799%3E3.0.CO;2-X)
- 701
- 702 Pomeroy, J. W., & Schmidt, R. A. (1993). The Use of Fractal Geometry in Modelling Inter-  
703 cepted Snow Accumulation and Sublimation. *Eastern Snow Conference*, 50, 231–239.
- 704 R Core Team. (2024). *R: A Language and Environment for Statistical Computing*. R Foun-  
705 dation for Statistical Computing. <https://www.r-project.org/>
- 706 Rittger, K., Raleigh, M. S., Dozier, J., Hill, A. F., Lutz, J. A., & Painter, T. H. (2020). Canopy  
707 Adjustment and Improved Cloud Detection for Remotely Sensed Snow Cover Mapping.  
708 *Water Resources Research*, 56(6), n/a. <https://doi.org/10.1029/2019WR024914>
- 709 Roesch, A., Wild, M., Gilgen, H., & Ohmura, A. (2001). A new snow cover fraction parame-  
710 terization for the ECHAM4 GCM. *Climate Dynamics*, 17(12), 933–946. <https://doi.org/10.1007/s003820100153>
- 711
- 712 Safa, H., Krogh, S. A., Greenberg, J., Kostadinov, T. S., & Harpold, A. A. (2021). Unraveling  
713 the Controls on Snow Disappearance in Montane Conifer Forests Using Multi-Site Lidar.  
714 *Water Resources Research*, 57(12), 1–20. <https://doi.org/10.1029/2020WR027522>
- 715 Satterlund, D. R., & Haupt, H. F. (1967). Snow catch by Conifer Crowns. *Water Resources  
716 Research*, 3(4), 1035–1039. <https://doi.org/10.1029/WR003i004p01035>
- 717 Schmidt, R. A., & Pomeroy, J. W. (1990). Bending of a conifer branch at subfreezing temper-  
718 atures: implications for snow interception. *Canadian Journal of Forest Research*, 20(8),  
719 1251–1253. <https://doi.org/10.1139/x90-165>
- 720 Schmidt, R. A., & Troendle, C. A. (1989). Snowfall into a forest and clearing. *Journal of  
721 Hydrology*, 110(3-4), 335–348. [https://doi.org/10.1016/0022-1694\(89\)90196-0](https://doi.org/10.1016/0022-1694(89)90196-0)
- 722 Smith, C. D. (2007). Correcting the wind bias in snowfall measurements made with a Geonor  
723 T-200B precipitation gauge and alter wind shield. *87th AMS Annual Meeting*.
- 724 Staines, J., & Pomeroy, J. W. (2023). Influence of forest canopy structure and wind flow  
725 on patterns of sub-canopy snow accumulation in montane needleleaf forests. *Hydrological  
726 Processes*, 37(10), 1–19. <https://doi.org/10.1002/hyp.15005>
- 727 Storck, P., Lettenmaier, D. P., & Bolton, S. M. (2002). Measurement of snow interception  
728 and canopy effects on snow accumulation and melt in a mountainous maritime climate,

- 729 Oregon, United States. *Water Resources Research*, 38(11), 1–16. <https://doi.org/10.1029/2002wr001281>
- 730
- 731 Troendle, C. A. (1983). The Potential for Water Yield Augmentation From Forest Management  
732 in the Rocky Mountain Region. *Journal of the American Water Resources Association*,  
733 19(3), 359–373. <https://doi.org/10.1111/j.1752-1688.1983.tb04593.x>
- 734 Valante, F., David, J. S., & Gash, J. H. C. (1997). Modelling interception loss for two sparse  
735 eucalypt and pine forests in central Portugal using reformulated Rutter and Gash analytical  
736 models. *Journal of Hydrology*, 190(1-2), 141–162. [https://doi.org/10.1016/S0022-1694\(96\)03066-1](https://doi.org/10.1016/S0022-1694(96)03066-1)
- 737
- 738 Van Stan, J. T., Siegert, C. M., Levia, D. F., & Scheick, C. E. (2011). Effects of wind-  
739 driven rainfall on stemflow generation between codominant tree species with differing crown  
740 characteristics. *Agricultural and Forest Meteorology*, 151(9), 1277–1286. <https://doi.org/10.1016/j.agrformet.2011.05.008>
- 741
- 742 Varhola, A., Coops, N. C., Weiler, M., & Moore, R. D. (2010). Forest canopy effects on  
743 snow accumulation and ablation: An integrative review of empirical results. *Journal of  
744 Hydrology*, 392(3-4), 219–233. <https://doi.org/10.1016/j.jhydrol.2010.08.009>
- 745
- 746 Vionnet, V., Mortimer, C., Brady, M., Arnal, L., & Brown, R. (2021). Canadian historical  
747 Snow Water Equivalent dataset (CanSWE, 1928–2020). *Earth System Science Data*, 13(9),  
748 4603–4619. <https://doi.org/10.5194/essd-13-4603-2021>
- 749
- 750 Watanabe, S., & Ozeki, J. (1964). Study of fallen snow on forest trees (II). Experiment on the  
751 snow crown of the Japanese cedar. *Jap. Govt. Forest Exp. Sta. Bull*, 169, 121–140.
- 752 Wheeler, K. (1987). *Interception and redistribution of snow in a subalpine forest on a storm-  
by-storm basis*. Western Snow Conference. <http://sites/westernsnowconference.org/PDFs/1987Wheeler.pdf>